It's about time: novel drug discovery concepts for the molecular pharmacological characterization fo the cannabinoid CB2 receptor
Bouma, J.

Citation

Bouma, J. (2024, September 11). *It's about time: novel drug discovery concepts for the molecular pharmacological characterization fo the cannabinoid CB2 receptor*. Retrieved from https://hdl.handle.net/1887/4082998

Version:	Publisher's Version
License:	
Downloaded from:	

Note: To cite this publication please use the final published version (if applicable).

Chapter 4

Structural basis of selective cannabinoid CB$_2$ receptor activation

🕱

Xiaoting Li*, Hao Chang*, Jara Bouma*, Laura V. de Paus, Partha Mukhopadhyay, Janos Paloczi, Mohammed Mustafa, Cas van der Horst, Sanjay Sunil Kumar, Lijie Wu, Yanan Yu, Richard J. B. H. N. van den Berg, Antonius P.A. Janssen, Aron Lichtman, Zhi-Jie Liu, Pal Pacher, Mario van der Stelt, Laura H. Heitman, Tian Hua

* These authors contributed equally.

Abstract

Cannabinoid CB$_2$ receptor (CB$_2$R) agonists are investigated as therapeutic agents in the clinic. However, their molecular mode-of-action is not fully understood. Here, we report the discovery of LEI-102, a CB$_2$R agonist, used in conjunction with three other CBR ligands (APD371, HU308 and CP55,940), to investigate the selective CB$_2$R activation by binding kinetics, site-directed mutagenesis, and cryo-EM studies. We identify key residues for CB$_2$R activation. Highly lipophilic HU308 and the endocannabinoids, but not the more polar LEI-102, APD371 and CP55,940, reach the binding pocket through a membrane channel in TM1-TM7. Favorable physico-chemical properties of LEI-102 enable oral efficacy in a chemotherapy-induced nephropathy model. This chapter delineates the molecular mechanism of CB$_2$R activation by selective agonists and highlights the role of lipophilicity in CB$_2$R engagement. This may have implications for GPCR drug design and sheds light on their activation by endogenous ligands.

4.1 Introduction

Preparations of the plant *Cannabis sativa* have been used for centuries in the treatment of various diseases, including cancer and neuropathic pain[1]. The synthetic version of its psychoactive constituent, Δ^9-tetrahydrocannabinol (THC, **Figure 4.1**), is in FDA approved drugs Marinol® or Syndros® (dronabinol). The extracted version of THC is one of the active constituents of oromucosal spray Sativex® (nabiximols). These drugs are primarily used for the treatment of chemotherapy-induced nausea, enhancement of appetite in cachexic AIDS-patients, and to alleviate the spasticity and pain associated with multiple scleroses[2–6]. However, THC-based therapies are associated with clinically undesired psychotropic and cardiovascular adverse effects and challenging pharmacokinetic properties due to their high lipophilicity that may limit their therapeutic efficacy[7–10].

THC exerts its therapeutic effects mostly via the G protein-coupled receptors (GPCRs) cannabinoid CB_1 and CB_2 receptors (CB_1R and CB_2R), which have 68% sequence identity in their seven transmembrane (TM) domains[11]. Both receptors are activated by the endogenous signaling lipids anandamide (AEA) and 2-arachidonoylglycerol (2-AG) (**Figure 4.1**), the two main endocannabinoids. The CB_1R, which is the most abundantly expressed GPCR in the central nervous system (CNS) is responsible for the psychotropic side effects of THC[12–14]. It plays a role in memory, learning, neurogenesis, neuronal migration, and synaptogenesis. Furthermore, its presence in many organ tissues belies more non-neurological functions[15]. The CB_2R is mainly found on the cells of the immune system and is upregulated under pathophysiological conditions[16,17]. Its activation in general is associated with anti-inflammatory responses in tissue injury of the liver, heart, kidney, colon, and brain as determined in various preclinical models[18–22]. Based on preclinical studies it is thought that selective CB_2R agonists may retain and exceed certain therapeutic properties of THC without inducing psychotropic side effects[23].

Various academic and industrial groups have developed selective CB_2R ligands[24]. HU308 (**Figure 4.1**) was the first selective CB_2R agonist to be reported that displayed anti-inflammatory and analgesic properties in mouse models without inducing CNS-side effects[18].
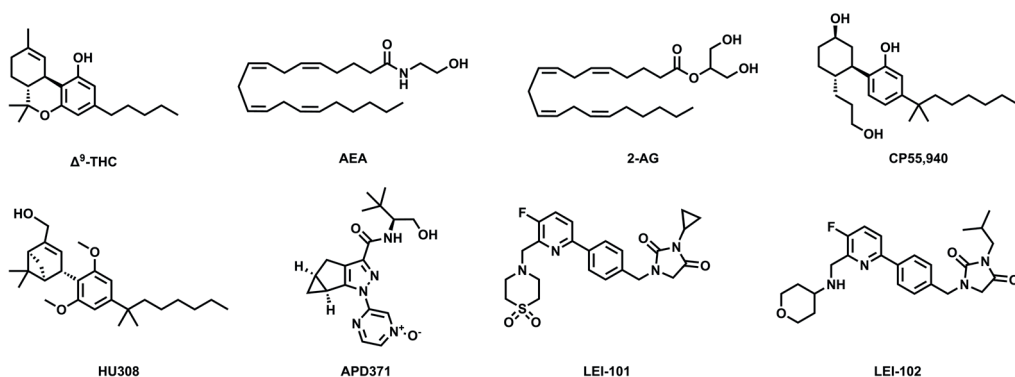
Figure 4.1 **Chemical structures.**

Shown are the main constituent of Cannabis sativa Δ^9-tetrahydrocannabinol (THC), and the two major endocannabinoids anandamide (AEA) and 2-arachidonoylglycerol (2-AG), as well as non-selective CBR agonist CP55,940 and CB_2R agonists HU308, APD371, LEI-101, and LEI-102.

However, poor physico-chemical properties (*e.g.* low solubility, high lipophilicity) of HU308, which has a calculated logarithm of octanol-water partition coefficient (cLogP) of 8.0[25], and its analogs prevented the successful clinical translation of this class of cannabinoid-based drugs.

A next generation of CB$_2$R ligands was developed with improved drug-like properties. For instance, Olorinab® (APD371, **Figure 4.1**) is the most polar CB$_2$R agonist reported to date with a cLogP of -0.4[26]. A phase 2a small-scale safety and tolerability trial in 14 patients with chronic abdominal pain associated with Crohn's disease showed mild-to-moderate adverse events and an improvement in abdominal pain scores[27]. We have previously disclosed pyridinylbenzylimidazolidine-2,4-dione derivatives as selective CB$_2$R agonists and studied their affinity, target binding kinetics and potency as a function of their lipophilicity, which resulted in the discovery of the orally available and peripherally restricted selective CB$_2$R agonist LEI-101 (**Figure 4.1**)[28–30]. It is intriguing that the CB$_2$R binding pocket tolerates a wide array of ligands with very different scaffolds and hydrophobicity. For example, HU308 has a 2-billion-fold higher lipophilicity than APD371. Despite the tremendous progress in the field of CB$_2$R drug discovery, we still do not have any molecular understanding on how these CB$_2$R agonists selectively activate CB$_2$R over CB$_1$R.

Recently, three-dimensional structures of the CB$_1$R and CB$_2$R have been elucidated in both the active and inactive states by crystallography or cryo-electron microscopy (cryo-EM) and the binding modes of diverse ligands and their activation mechanism were reported[31–35]. Remarkably, those structures revealed that CB$_1$R and CB$_2$R possess a highly similar, lipophilic orthosteric agonist binding pocket, which makes it challenging to explain the selective activation of CB$_2$R. To date, no structural studies with selective CB$_2$R agonists have been reported that could aid in understanding the molecular basis of CB$_2$R selectivity.

Here, we present the discovery of LEI-102, a potent and selective CB$_2$R agonist with good physicochemical and biological properties. LEI-102 is used in conjunction with CB$_2$R selective agonists APD371 and HU308, and nonselective agonist CP55,940 to investigate the activation mechanism of CB$_2$R. For this study, we combine ligand-target binding kinetics, site-directed mutagenesis, and cryo-EM methods. We find that CB$_2$R has a distinct activation mechanism compared to CB$_1$R. Additionally, we find that the physico-chemical properties of the ligands influence their entry pathway into the receptor. Highly lipophilic ligands, such as HU308 and the endocannabinoids, may reach the binding pocket through the membrane, whereas more polar ligands, such as LEI-102, APD371 and CP55,940, enter the receptor via an alternative route. Furthermore, we show that the favorable physico-chemical properties of LEI-102 and CB$_2$R selectivity underscore its promising *in vivo* efficacy via oral administration in a chemotherapy-induced nephropathy model without inducing CNS-mediated side effects. Together, these studies enhance our insights into how certain physicochemical properties of ligands translate to *in vivo* activity and changes their engagement to GPCRs.

4.2 Results

4.2.1 LEI-102 as a high affinity and potent CB₂R-selective agonist

To obtain a selective CB_2R agonist with beneficial physico-chemical properties, LEI-102, a pyridinylbenzylimidazolidine-2,4-dione derivative, was designed and synthesized (**Figure 4.S1**). LEI-102 combined an isobutyl substituent on the imidazolidine with an aminotetrahydropyran to replace the cyclopropyl and thiomorpholine 1,1-dioxide in LEI-101, respectively[30]. LEI-102 had a cLogP of 2.1 as calculated by ChemDraw 19.0 (**Table 4.S1**). The inhibitory constant (pK_i), potency (pEC_{50}) and intrinsic activity (E_{max}) of LEI-102 were determined in [³H]RO6957022 displacement assays on stably expressing CB_2R membranes and [³⁵S]GTPγS G protein activation assays using HEK293T membranes transiently expressing recombinant hCB_2R or hCB_1R, respectively (**Table 4.S2**). APD371, HU308, CP55,940 and the endocannabinoids AEA and 2-AG were also explored. LEI-102 had a high binding affinity for CB_2R (pK_i 8.0 ± 0.1) and was more potent than the selective CB_2R agonists APD371 and HU308. LEI-102 did not bind CB_1R, thereby showing at least 1000-fold selectivity (**Table 4.S3**). In G protein activation assays, LEI-102 activated the receptor as a partial agonist (E_{max} 76 ± 1 %) with a pEC_{50} value of 6.9 ± 0.2 (**Table 4.S2**).

4.2.2 Distinct target binding kinetic profiles of CB₂R agonists

To quantify the ligand-target binding kinetic parameters of the agonists in more detail, we performed displacement and competition association assays with [³H]RO6957022 on membranes stably expressing hCB_2R (**Table 4.S2**). The equilibrium K_i and kinetic K_D values were well correlated, validating the competition association assay. First, we determined the dissociation rate constants (k_{off}) of all agonists and converted these into a residence time (RT). LEI-102 had a RT of 16 min, which was around half that of APD371 (45 min) and CP55,940 (32 min), whereas HU308 had the longest RT at the receptor of 71 min (**Table 4.S2**). Endocannabinoids 2-AG and AEA had the shortest RT, both approximately 7 min. Of note, we found that the association rate constants (k_{on}) varied greatly between the different agonists, ranking from fast to slow engagement CP55,940 > LEI-102 > 2-AG > APD371 > HU308 = AEA. The calculated engagement time (ET) to CB_2R at 1 μM of each agonist further emphasized that CP55,940 arrived at CB_2R within one second, whereas APD371, LEI-102 and 2-AG needed between 16 and 40 s to reach the CB_2R binding site. Interestingly, HU308 and AEA took 143 and 152 s to bind CB_2R, respectively. In view of the distinct target-binding kinetic profiles of the four synthetic CB_2R agonists, we decided to elucidate their binding poses in the CB_2R using cryo-EM.

4.2.3 Overall similar structural comparison of CB₂R-Gᵢ in complex with different agonists

To obtain the stable complex sample of CB_2R-G_i bound with LEI-102, APD371, HU308, or CP55,940, a similar procedure was used as for our previous AM12033-CB_2R-G_i complex preparation (PDB: 6KPF). Single particle analysis of the cryo-EM samples yielded a normal global map for CB_2R-LEI-102-G_i-scFv16, CB_2R-APD371-G_i-scFv16, CB_2R-HU308-

G$_i$-scFv16 and CB$_2$R-CP55,940-G$_i$-scFv16, complex, at 2.9 Å, 3.0 Å, 3.0 Å and 2.9 Å, respectively (**Figure 4.2**, **4.S2-4.S5**, **Table 4.S4**). The ligand, receptor and G protein in the isolated complex were clearly visible in the cryo-EM maps (**Figure 4.2**, **4.S6**). The overall structures of the four complexes were comparable, with root mean square deviation (RMSD) of the Cα atoms of the receptors are around 0.35 Å. The ligand binding interfaces of the four CB$_2$R and G$_i$ complexes were similar to each other, and to those of the previous AM12033-CB$_2$R-G$_i$ or WIN55212-2-CB$_2$R-G$_i$ complex structures.

### 4.2.4 The binding mode of LEI-102 in CB$_2$R

A clear electron density in the orthosteric ligand binding pocket in the LEI-102-CB$_2$R-G$_i$ complex resulted in the unambiguously defined binding pose of LEI-102 (**Figure 4.S6a**). LEI-102 predominantly interacted with the residues in the binding pocket via hydrophobic interactions (**Figure 4.3a**, **4.S7a**). The isobutyl substituent of LEI-102 showed interactions with residues S90$^{2.60}$ (Ballesteros-Weinstein numbering in superscript), F106$^{3.25}$, K109$^{3.28}$, and I110$^{3.29}$ in CB$_2$R. The imidazolidine-2,4-dione forms π-π interaction with F94$^{2.64}$ and showed further hydrophobic interactions with F106$^{3.25}$ and P184^{ECL2}. The benzyl formed an aromatic interaction with F183^{ECL2}, and hydrophobic interactions with F87$^{2.57}$ and S285$^{7.39}$. The phenyl ring in the core of LEI-102 formed a cationπ interaction with F183^{ECL2} and T-shaped π-π interaction with F281$^{7.35}$. The pyridine had hydrophobic contacts with F117$^{3.36}$ and W258$^{6.48}$. The aminotetrahydropyran sidechain protruded into the long channel and formed hydrophobic interactions with residues I110$^{3.29}$, T114$^{3.33}$, I186^{ECL2}, Y190$^{5.39}$, L191$^{5.40}$, W194$^{5.43}$ and M265$^{6.55}$. Additionally, a hydrogen bond was formed with T114$^{3.33}$ (**Figure 4.S7a**).

4.2.5 The binding mode of APD371 in CB$_2$R

APD371 mainly formed hydrophobic and aromatic interactions with residues from ECL2, TM2, TM3, TM5, TM6 and TM7 (**Figure 4.3b**, **4.S7b**). The carbonyl group of APD371 formed a putative hydrogen bond with S285$^{7.39}$ and a hydrophobic interaction with F87$^{2.57}$. The pyrazole and pyrazine cores of APD371 formed aromatic interaction with F183^{ECL2}. Furthermore, the pyrazine core formed hydrophobic contacts with T114$^{3.33}$, I186^{ECL2}, L191$^{5.40}$ and W194$^{5.43}$. The (*S*)-1-hydroxy-3,3-dimethylbutyl head formed hydrophobic contacts with residues M26$^{N-terminus}$, S90$^{2.60}$, F94$^{2.64}$, F106$^{3.25}$, I110$^{3.29}$ and V113$^{3.32}$. The cyclopropyl group formed hydrophobic contacts with F117$^{3.36}$, W194$^{5.43}$, W258$^{6.48}$ and V261$^{6.51}$.

4.2.6 The binding mode of HU308 in CB$_2$R

The interactions between HU308 and CB$_2$R were hydrophobic, including residues from ECL2, TM2, TM3, TM5, TM6 and TM7 (**Figure 4.3c**, **4.S7c**). The phenyl of 2,6-dimethoxyphenyl core formed hydrophobic interactions with F87$^{2.57}$, F183^{ECL2} and S285$^{7.39}$, the C2-methoxy formed hydrophobic contacts with A282$^{7.36}$ and S285$^{7.39}$, and the C6-methoxy formed
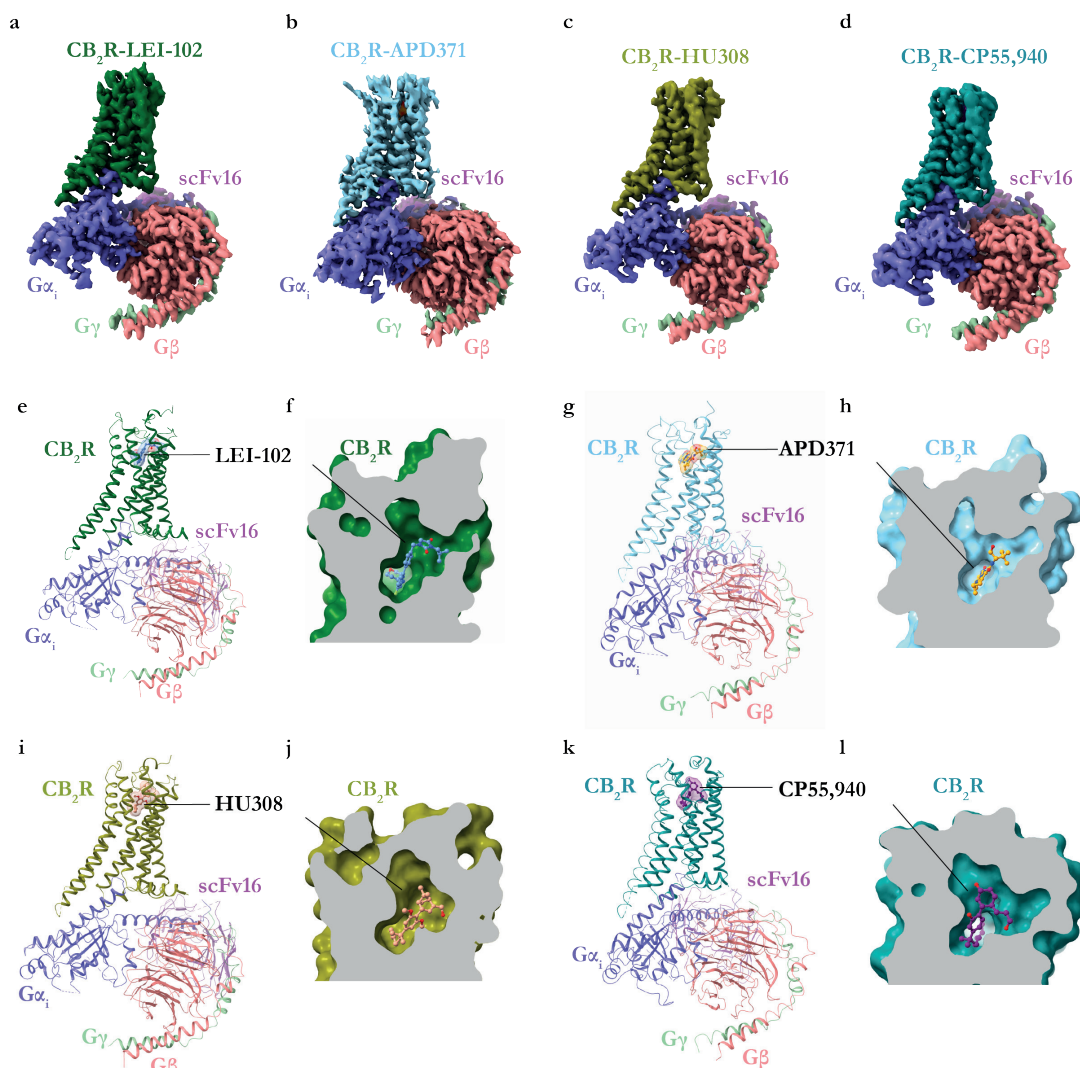
Figure 4.2   Cryo-EM structures of CB$_2$R-G$_i$ complexes.
Cryo-EM density maps of (a) LEI-102 (Dark green), (b) APD371 (Sky blue), (c) HU308 (Olive), and (d) CP55,940 (Teal) bound CB$_2$R in complex with Gα$_i$ (Slate), Gβ (Salmon), Gγ (Pale green), scFv16 (Violet purple). (e–l) Overall structures of CB$_2$R-G$_i$ complexes and enlarged view of orthosteric pocket of (f) LEI-102, (h) APD371, (j) HU308, and (l) CP55,940 using the same color codes as (a–d), with agonists shown as cornflower blue (LEI-102), orange (APD371), dark salmon (HU308) and purple (CP55,940) sticks, respectively.

hydrophobic contacts with I110$^{3.29}$, V113$^{3.32}$ and T114$^{3.33}$, respectively. The dimethylheptyl chain of HU308 extended into the long channel and formed hydrophobic interactions with residues from ECL2 (F183^{ECL2}), TM3 (T114$^{3.33}$, F117$^{3.36}$), TM5 (W194$^{5.43}$). The 1,1-dimethyl formed hydrophobic interactions with residues F87$^{2.57}$, F117$^{3.36}$, F281$^{7.35}$ and S285$^{7.39}$. The bicyclic head of HU308 formed hydrophobic interactions with M26$^{N\text{-terminus}}$, F106$^{3.25}$, I110$^{3.29}$, S90$^{2.60}$, F94$^{2.64}$, P184^{ECL2} and the 2-methanol formed a hydrophobic interaction with F94$^{2.64}$ (**Figure 4.S7c**).

### 4.2.7   The binding mode of CP55,940 in CB$_2$R

CP55,940 adopted an L-shape conformation in the orthosteric binding pocket (**Figure 4.3d**, **4.S6d**). The cyclohexanol group formed hydrophobic interactions with F94$^{2.64}$, L182^{ECL2}, F183^{ECL2}, and P184^{ECL2}. The hydroxyl group established a hydrogen bond with L182^{ECL2} and the hydroxypropyl formed hydrophobic contacts with F87$^{2.57}$, S90$^{2.60}$, F91$^{2.61}$, I110$^{3.29}$, and V113$^{3.32}$. The phenol core formed hydrophobic interactions with F87$^{2.57}$, F183^{ECL2}, F281$^{7.35}$ and S285$^{7.39}$, and its hydroxyl additionally formed a hydrogen bond with S285$^{7.39}$. The dimethyl formed hydrophobic interactions with F183^{ECL2}, F281$^{7.35}$, M265$^{6.55}$, F87$^{2.57}$, F117$^{3.36}$ and C288$^{7.42}$. The dimethylheptyl alkyl chain of CP55,940 extended into the long channel and formed hydrophobic interactions with residues I110$^{3.29}$, F183^{ECL2}, I186^{ECL2}, W194$^{5.43}$, T114$^{3.33}$ and F117$^{3.36}$ (**Figure 4.S7d**).

4.2.8   LEI-102 and APD371 require H95$^{2.65}$ for G Protein activation in CB$_2$R

To study the mechanism of CB$_2$R activation, five residues in the binding pocket were further characterized based on the complex structures (**Figure 4.3**). Six CB$_2$R mutants were created, *i.e.* four residues (S285$^{7.39}$, H95$^{2.65}$, I110$^{3.29}$ and F117$^{3.36}$) were replaced by alanine, as these are conserved between CB$_2$R and CB$_1$R, and two others (I110$^{3.29}$, V261$^{6.51}$) were substituted by the hCB$_1$R reciprocal residue leucine. All mutants were sufficiently expressed at the cell surface as determined with an ELISA (**Figure 4.S8**, **Table 4.S5**). To characterize the binding mechanisms of LEI-102, APD371, HU308 and CP55,940, their responses were investigated by [^{3}H]CP55,940 displacement and [^{35}S]GTPγS binding assays. Of note, in the [^{3}H]CP55,940 displacement assay, only the CB$_2$R-I110$^{3.29}$L mutant showed a sufficient binding window (data not shown). This prevented the affinity determination of the four agonists on other mutant receptors. Five mutant receptors, except CB$_2$R-F117$^{3.36}$A, were still active in the [^{35}S]GTPγS functional assay, thereby allowing us to study the receptor activation mechanism (**Figure 4.4a-d**, **Table 4.S6**). All four synthetic agonists were unable to activate CB$_2$R-F117$^{3.36}$A, which indicated an important role of this residue in the activation of CB$_2$R.

The potency of LEI-102 was significantly increased at the CB$_2$R-I110$^{3.29}$L mutant to a pEC$_{50}$ value of 7.8 ± 0.1 in the G protein activation assay, while the binding affinity remained similar to wild type (WT) receptor (**Figure 4.4a**, **Table 4.S6**, **4.S7**). Three mutations CB$_2$R-I110$^{3.29}$A, CB$_2$R-S285$^{7.39}$A and CB$_2$R-V261$^{6.51}$L had no significant effect on the potency of LEI-102 in the functional assay. In contrast, the potency on mutant receptor CB$_2$R-H95$^{2.65}$A was significantly reduced for LEI-102. No gain in binding affinity for the swap mutant in CB$_1$R-L359$^{6.51}$V was found with LEI-102 (**Table 4.S3**, **4.S8**).

APD371 acted as a full CB$_2$R agonist with a pEC$_{50}$ value of 7.9 ± 0.1 and a higher maximal activation compared to that of CP55,940 in the functional assay (**Table 4.S2**). Mutant receptor CB$_2$R-I110$^{3.29}$L did not affect the G protein response of APD371 (**Figure 4.4b**, **Table 4.S6**), while the binding affinity was significantly reduced to a pK$_i$ of 7.1 ± 0.0 (**Table 4.S7**). APD371 potency was not affected by mutant receptors CB$_2$R-I110$^{3.29}$A or CB$_2$R-S285$^{7.39}$A. The responses of APD371 for CB$_2$R-H95$^{2.65}$A and CB$_2$R-V261$^{6.51}$L were significantly impacted with 158-fold and 10-fold drop in potency, respectively (**Table 4.S6**).
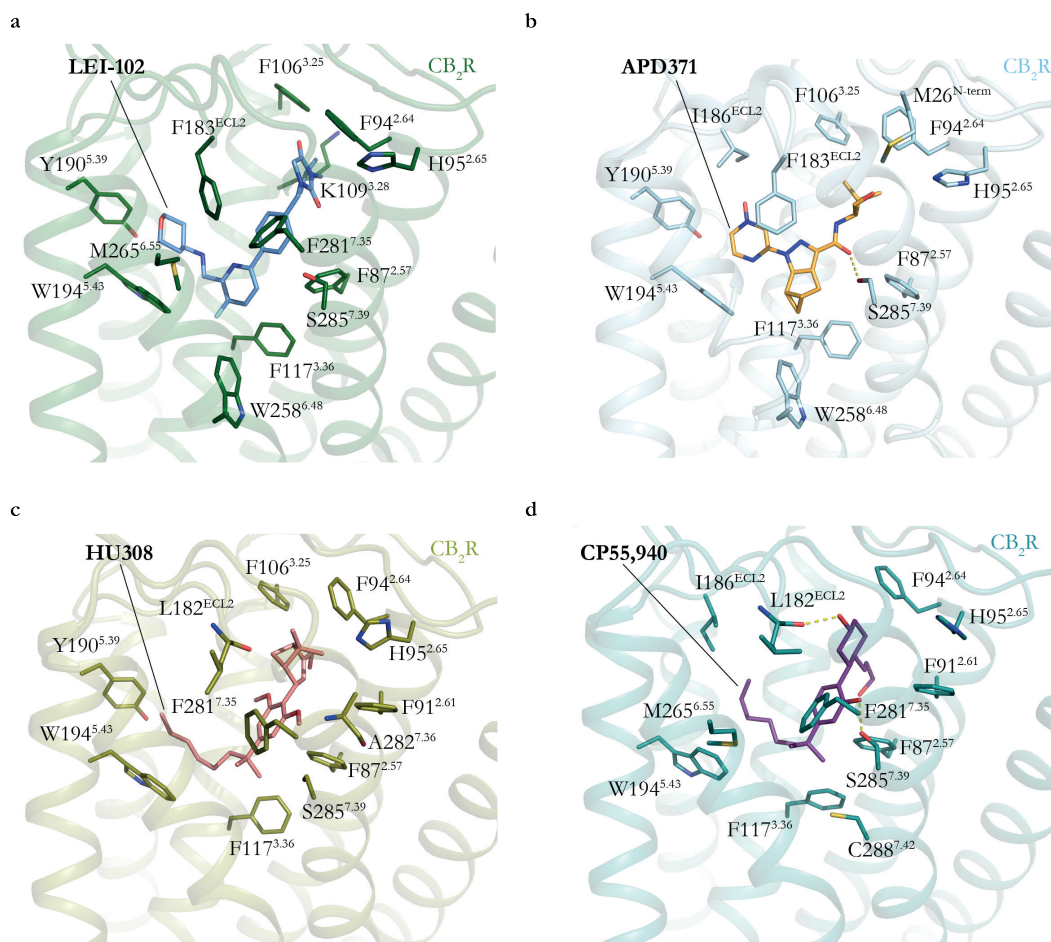
Figure 4.3 **Key interactions between CB$_2$R and agonists.**
Key residues involved in **a** LEI-102, **b** APD371, **c** HU308, and **d** CP55,940 binding in CB$_2$R-G$_i$ complex structures. The amino acids involved in interactions are shown as sticks, hydrogen bonds are highlighted with yellow dashed lines. Same color codes as in **Figure 4.2**.

Thus, we uncovered a crucial role for CB$_2$R-H95$^{2.65}$ in G protein activation of CB$_2$R by LEI-102 and APD371. It's role in stabilizing Furthermore, LEI-102 activation was increased for the CB$_2$R-I110$^{3.29}$L mutant, while APD371 activation relied on CB$_2$R-V261$^{6.51}$.

4.2.9 *An important role for S285$^{7.39}$ and V261$^{6.51}$ in CB$_2$R activation by HU308 and CP55,940*

The potency and affinity of HU308 on CB$_2$R were not affected by the CB$_2$R-I110$^{3.29}$L swap mutant (**Figure 4.4c**, **Table 4.S6**, **4.S7**). In addition, activation of mutant receptors CB$_2$R-I110$^{3.29}$A and CB$_2$R-H95$^{2.65}$A by HU308 was not affected with pEC$_{50}$ values of 6.4 ± 0.5 and 6.6 ± 0.6, respectively. The maximum activation level of mutant receptor CB$_2$R-S285$^{7.39}$A was unaffected compared to WT receptor, but a significant 15-fold loss in potency was

observed. Lastly, CB$_2$R-V261$^{6.51}$L had a significant loss of potency, *i.e.* more than 120-fold lower (**Figure 4.4c**, **Table 4.S6**).

Similar to HU308, the potency of CP55,940 on CB$_2$R was not affected by the CB$_2$R-I110$^{3.29}$ mutations compared to WT in the G protein activation assay, nor was its binding affinity for CB$_2$R-I110$^{3.29}$L (**Figure 4.4d**, **Table 4.S6**, **4.S7**). In response to CP55,940, mutant receptors CB$_2$R-S285$^{7.39}$A and CB$_2$R-V261$^{6.51}$L were significantly affected with decreased pEC$_{50}$ values of 6.7 ± 0.1 and <5, respectively. Moreover, the potency of CP55,940 was significantly affected on the CB$_2$R-H95$^{2.65}$A with a 40-fold decrease compared to WT receptor (**Figure 4.4d**, **Table 4.S6**). No gain in potency or affinity was observed for the swap mutant CB$_1$R-L359$^{6.51}$V for either HU308 or CP55,940 (**Table 4.S3**, **4.S8**).

Taken together, this showed that CB$_2$R-S285$^{7.39}$ and CB$_2$R-V261$^{6.51}$ were crucial for HU308 and CP55,940 to activate the G protein at CB$_2$R, where CP55,940 additionally required an interaction with CB$_2$R-H95$^{2.65}$.

4.2.10 *HU308 and endocannabinoids gain access via membrane entry*

Our detailed ligand-target binding kinetic analysis revealed that the highly lipophilic HU308 and anandamide had a very slow on-rate compared to the other ligands. Since it has previously been postulated that ligands of lipid receptors may gain access to the binding pocket via a membrane channel, we examined two potential ligand entry pathways at CB$_2$R, *i.e.* either via ECL2 or via a membrane channel in TM1 and TM7. To this end, four additional mutant receptors were created. Three residues in the ECL2 of CB$_2$R, which were different from CB$_1$R, were mutated towards the reciprocal CB$_1$R residues, *i.e.* CB$_2$R-L185^{ECL2}H, CB$_2$R-L182^{ECL2}I and CB$_2$R-E181^{ECL2}D. In the fourth mutant receptor, four residues in TM1 and TM7 that align the potential membrane channel in CB$_2$R were mutated to the reciprocal CB$_1$R residues and combined as a quadruple mutant, *i.e.* CB$_2$R-K279$^{7.33}$T, CB$_2$R-K33$^{1.32}$Q, CB$_2$R-V36$^{1.35}$I and CB$_2$R-C40$^{1.39}$S (termed "CB$_2$R-Quadruple^{TM1,7}"). Next, we tested all four synthetic agonists and the two endocannabinoids on these four CB$_2$R mutant receptors in [^{3}H]CP55,940 and [^{35}S]GTPγS assays. Only CB$_2$R-L185^{ECL2}H and CB$_2$R-Quadruple^{TM1,7} were evaluated in the [^{3}H]CP55,940 displacement assays due to insufficient binding window for the other two mutant receptors (data not shown). The binding affinities of the agonists were not affected for mutant receptors CB$_2$R-L185^{ECL2}H and CB$_2$R-Quadruple^{TM1,7} (**Table 4.S7**). Interestingly, the potencies of LEI-102, APD371 and CP55,940 in the functional assay were not significantly affected for any of the mutant receptors, whereas HU308 and the endocannabinoids were less potent on CB$_2$R-L182^{ECL2}I (**Figure 4.4e-j**, **Table 4.S6**). Additionally, the endocannabinoids showed a decreased potency on CB$_2$R-L181^{ECL2}D, but not on CB$_2$R-L185^{ECL2}H. Of note, HU308 and both endocannabinoids completely lost their ability to activate CB$_2$R in the CB$_2$R-Quadruple^{TM1,7} mutant, suggesting that this may be an important access point to the receptor binding pocket for these agonists (**Figure 4.4g,i-j**).
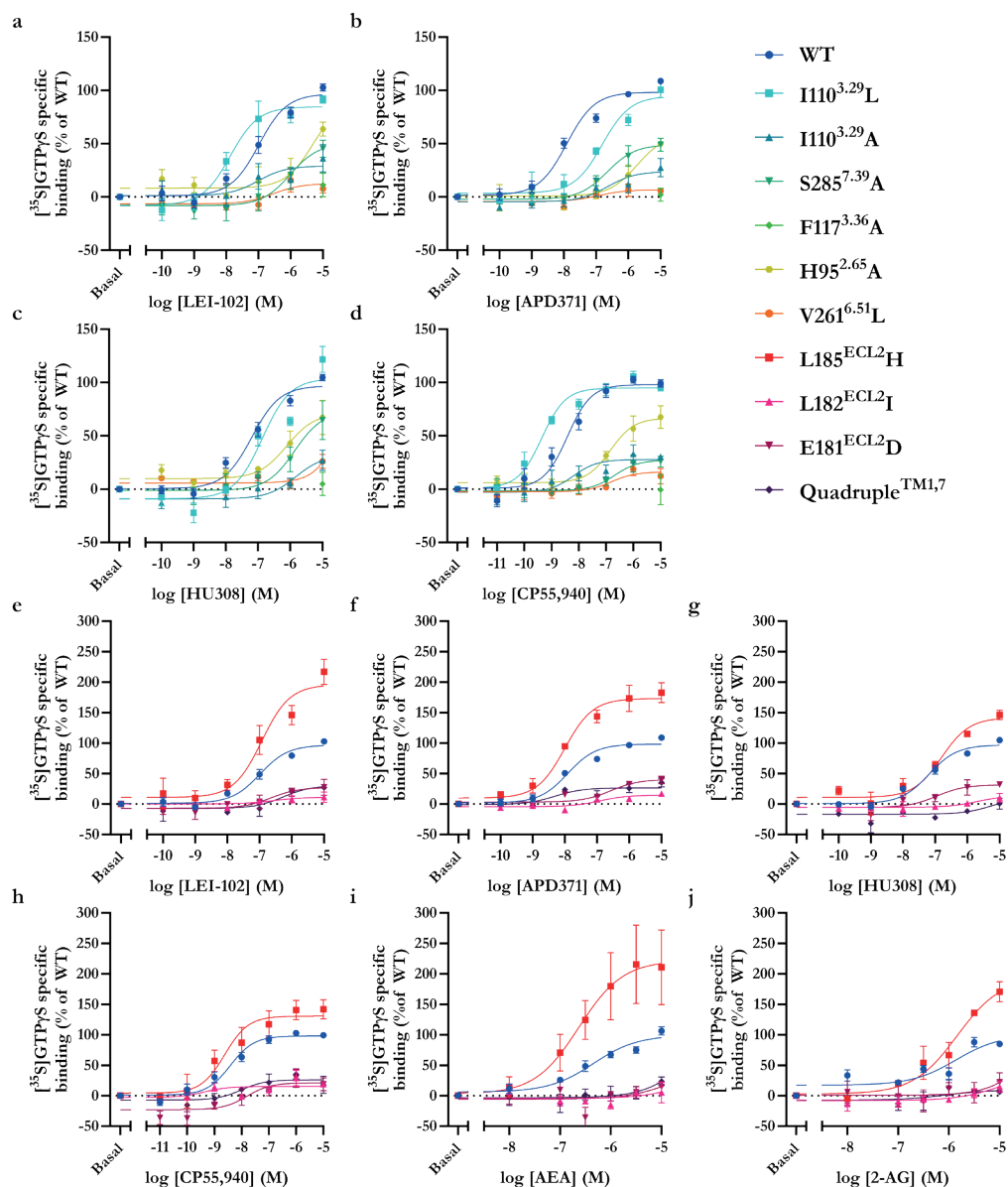
Figure 4.4   Characterization of G protein activation of wild type (WT) and mutant CB₂R by synthetic agonists and endocannabinoids.
Dose-response curves for G protein activation of WT and mutants that are located in the CB₂R binding pocket by (a) LEI-102, (b) APD371, (c) HU308, and (d) CP55,940. (e–j) Dose response curves for G protein activation of WT and mutants that are proposed to be involved in ligand entry of CB₂R via either the ECL2 or membrane access by (e) LEI-102, (f) APD371, (g) HU308, (h) CP55,940, (i) AEA and (j) 2-AG. (a–j) The maximum activation level of WT CB2R was set to 100% while the basal levels were set to 0%. Data are presented as mean ± SEM of at least three individual experiments performed in duplicate.

### 4.2.11 *LEI-102 attenuates cisplatin-induced nephrotoxicity without CB$_1$R-mediated side effects*

In view of the excellent physico-chemical properties of LEI-102 and its selective CB$_2$R agonist profile, we investigated the compound in a well-established *in vivo* model of kidney inflammation and injury induced by cisplatin. In this model CB$_2$R activation is associated with protective effects[29]. Cisplatin (25 mg/kg, i.p.) induced marked elevations of serum creatinine and blood urea nitrogen levels (functional markers of kidney injury) 72 h following cisplatin injection in wild type mice compared with vehicle-treated control animals. LEI-102 showed a dose-dependent attenuation of the functional markers of cisplatin-induced kidney injury both when administered p.o. (orally) or i.p. (**Figure 4.5a**). Renal dysfunction was also accompanied by morphological damage to the kidney tubules determined by histological examination following PAS staining. LEI-102 (10 mg/kg) significantly decreased tubular injury as determined by this staining (**Figure 4.5b**). Marked increases in oxidative and nitrative stress markers (4-HNE and 3-nitrotyrosine) were observed in kidneys of cisplatin-treated mice determined by immunostaining and quantitative ELISA. Furthermore, LEI-102 (10 mg/kg by i.p. or p.o.) decreased lipid peroxidation and protein nitration (**Figure 4.5c,d**). Additionally, the pro-inflammatory cytokines TNFα and IL1β that were elevated due to the cisplatininduced injury were attenuated in LEI102 treated mice (**Figure 4.5e**). Importantly, the protective effects of LEI-102 against cisplatin-induced renal dysfunction and tubular damage (**Figure 4.5f**), histopathological injury (**Figure 4.5g**) and markers of oxidative-nitrative stress (**Figure 4.5h,i**) were abolished in CB$_2$R knockout mice, which had enhanced kidney injury/dysfunction compared to their wild types.

To determine whether LEI-102 maintained its selectivity for CB$_2$R over CB$_1$R *in vivo*, LEI-102 was tested in the mouse tetrad assay for CB$_1$R activity[18]. In this assay, four consecutive behavioral tests, related to anti-nociception, hypothermia, catalepsy, and spontaneous activity, were performed 120 min after administration of the agonist. LEI-102 (25 mg/kg, p.o.) did not produce any effects in the tetrad assay as compared with vehicle. There were no effects on nociceptive behavior assessed in tail withdrawal test nor on body temperature

→ **Figure 4.5** **CB$_2$R agonist LEI-102 attenuates cisplatin-induced renal dysfunction, oxidative stress, and inflammation in a CB$_2$R-dependent manner.**
(a) Cisplatin-induced renal dysfunction 72 h after administration to mice as evidenced by increased serum levels of blood urea nitrogen (BUN) and creatinine (CREA), which were attenuated by CB$_2$R agonist LEI-102 in a dose-dependent manner when administered either i.p. or p.o. (*$p < 0.001$ vs. vehicle group, #$p < 0.001$ vs. cisplatin group). (b) Periodic Acid-Schiff (PAS) staining in representative kidney sections from cisplatin treatment samples showing protein cast, vacuolation, and desquamation of epithelial cells in the renal tubules which are attenuated with LEI-102. Tubular damage score from kidney sections is shown (*$p < 0.001$ vs. vehicle group, #$p < 0.001$ vs. cisplatin group). (c) The cisplatin-induced nitrative and oxidative stress (nitrotyrosine staining (top row) and HNE staining (bottom row)) in representative kidney sections were also attenuated by LEI-102. (d) This was confirmed by quantitative determination of protein nitration and HNE adducts formation by ELISA (*$p < 0.001$ vs. vehicle group, #$p < 0.001$ vs. cisplatin group). (e) The cisplatin-induced kidney pro-inflammatory cytokine expressions were also attenuated by the CB2R agonist. (*$p < 0.001$ vs. vehicle group, #$p < 0.05$ vs. cisplatin group). (f) The protective effects of LEI-102 on cisplatin-induced kidney dysfunction (BUN and CREA) and tubular injury (tubular damage score) (*$p < 0.001$ vs. vehicle WT or KO group, #$p < 0.05$ vs. cisplatin WT group), histopathological injury (g), nitrative (h) and oxidative stress (i) were abolished in CB$_2$R knockout mice. All results are means ± SEM of n = 6/group for panels (a, b, d, e, f). Closed and open symbols are used for male and female mice respectively (4 males and 2 females/group). In panels (a, b, d), and (e) one-way ANOVA followed by Tukey's post hoc test for multiple comparisons were used, in panel f unpaired two-tailed t-test was used. $p < 0.05$ was considered statistically significant.

(**Figure 4.6 upper row**). No effect was found on locomotor behavior (**Figure 4.6 lower row**) in case of distance travelled, time spent mobile, or running speed of mice. Nor was catalepsy observed following administration of LEI-102. These results indicated that LEI-102 (or one of its metabolites) did not produce CB_1R-mediated CNS-side effects at doses up to 25 mg/kg (p.o.). Hence, the CB_2R agonist LEI-102 maintained its selectivity over CB_1R *in vivo*.

117
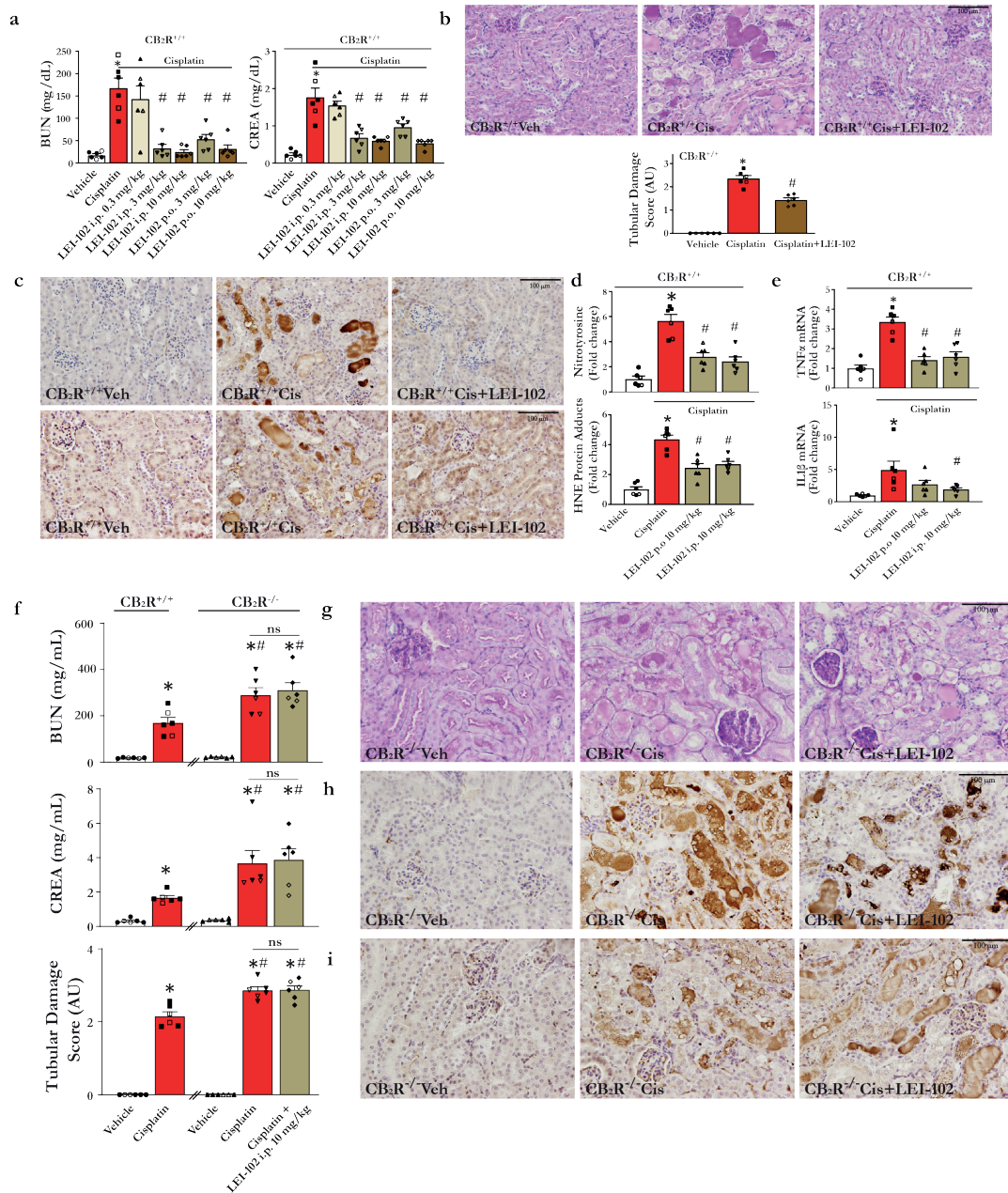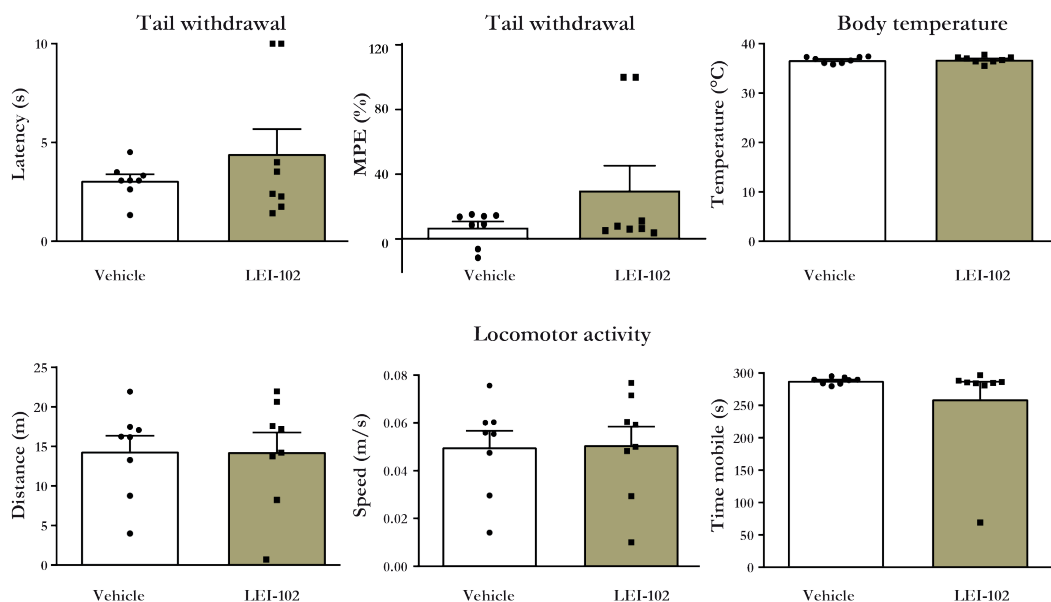
Figure 4.6 **The CB$_2$R agonist LEI-102 does not induce cannabimimetic CB$_1$R-mediated effects (Tetrad assay)** *in vivo.*
LEI-102 (25 mg/kg, p.o.) did not affect nociceptive behavior assessed in tail withdrawal test and body temperature, as compared with mice receiving vehicle (upper row). No effects on locomotor behavior were found (lower row). Results are means ± SEM; n = 8 per group.

4.3   Discussion

So far, several crystal and cryo-EM CBR structures have been resolved in which non-selective agonists adopt a nearly identical binding position in the orthosteric pocket, regardless of the receptor[34–38]. In this study, we aimed to generate a better understanding of the binding and activation mechanism of CB$_2$R-selective agonists. Therefore, we combined ligand-target binding kinetics, site-directed mutagenesis, and cryo-EM studies to investigate the activation mechanism of CB$_2$R for the introduced CB$_2$R selective agonist LEI-102 supplemented with agonists APD371, HU308 and CP55,940 on a molecular level. Furthermore, we investigated potential hotspots for CB$_2$R/CB$_1$R selectivity by creating swap mutants and discovered a ligand entry pathway for CBR agonists and endocannabinoids.

First, our data revealed a crucial role for CB$_2$R-F117$^{3.36}$ as replacement by alanine resulted in a complete loss of G protein activation by all tested agonists (**Figure 4.4a-d**, **Table 4.S6**). It has been shown that the CB$_1$R counterpart F200$^{3.36}$ plays an important regulatory role in activation as part of the "twin toggle switch" with CB$_1$R-W356$^{6.48}$ [39]. In contrast, CB$_2$R-W258$^{6.48}$ has been described to be solely responsible for activation as a toggle switch without the help of CB$_2$R-F117$^{3.36}$ in structural studies, since the conformation of CB$_2$R-F117$^{3.36}$ in agonist-bound structures is comparable to the conformation in the antagonist-bound CB$_2$R structure as well as the CB$_1$R agonist-bound structures[33,36]. Our mutational data further supports this hypothesis, as we do not see the same constitutive

activity pattern (**Table 4.S6**) as observed by McAllister *et al.* for the reciprocal CB_1R-$F220^{3.36}$ excluding CB_2R-$F117^{3.36}$ from a suppressive function[39]. Together, this data provides strong support for a different, but important, role for $F117^{3.36}$ in CB_2R activation.

In CB_1R, water-mediated interactions between CB_1R-$H178^{2.65}$, CB_1R-$S383^{7.39}$ and bound ligands have previously been shown with *in silico* modelling[40,41]. The importance of CB_1R-$S383^{7.39}$ for classical synthetic cannabinoids such as AM11542, AM841 and CP55,940 was further emphasized in CB_1R-$S383^{7.39}A$ mutants[36]. This is in line with the observation that removal or methylation of the phenolic OH on classical cannabinoids, such as in L-759656, JWH-133 and HU308, always affords selectivity over $CB_1R^{18,42}$. Non-classical agonists, such as WIN55,212-2, do not form a hydrogen bond with CB_1R-$S383^{7.39}$ and consequently are not affected by an alanine mutation[43]. This translates to our results that CP55,940 and HU308 are more affected by the CB_2R-$S285^{7.39}A$ mutation than LEI-102 and APD371 (**Figure 4.4a-d**, **Table 4.S3**). The decrease in activation is at least 30-fold smaller for CB_2R than CB_1R^{36}. The elucidated cryo-EM structures of our four agonists did not show direct interactions with CB_2R-$H95^{2.65}$, though we cannot rule out its role in stabilizing the surrounding residues. The large effect seen on G protein activation of CB_2R-$H95^{2.65}A$ by LEI-102, APD371 and CP55,940 (**Figure 4.4a-d**, **Table 4.S6**) must therefore stem from an indirect interaction, supporting the polar network hypothesis between CB_2R-$H95^{2.65}$ and CB_2R-$S285^{7.39}$ in CB_2R.

Residues at position 6.51 have previously been described to be involved in the binding sites of μ, δ, and κ opioid receptors, the dopamine D2 receptor and adenosine receptors, and could play a role in ligand binding selectivity between different subtypes[44–46]. In our studies, introduction of the bulkier CB_1R leucine on this position in CB_2R-$V261^{6.51}L$ reduced the G protein activation by APD371, HU308 and CP55,940, while LEI-102 could still be accommodated in the binding pocket (**Figure 4.4a-d**, **Table 4.S6**). Furthermore, with the swap mutant CB_1R-$L359^{5.61}V$ we found a trend in partial recovery of displacement of [³H]CP55,940 by the CB_2R selective agonists LEI-102, HU308 and APD371, although not significant (**Table 4.S3**). This supports a role of this residue in selectivity of agonists in CB_2R.

The ECL2 has frequently been implicated to be important for GPCR activation and some GPCRs even use their ECL2 as a ligand to auto-activation[47]. There are distinct differences between the conformations of ECL2 in CB_1R and CB_2R. In antagonist-bound CB_1R crystal structures, the ECL2 dips into the binding pocket, interacting with the ligand and inducing the inactive conformation[31,32]. The inactive state of CB_2R, however, does not expand like CB_1R and instead the ECL2 acts more as a lid on the binding pocket in active and inactive CB_2R, akin to active CB_1R^{33}. A key distinction seen in the CB_1R crystal structures with AM6538 and taranabant, is the ionic lock formed by CB_1R-$E100^{N-terminus}$ (CB_2R-L17) and CB_1R-$H270^{ECL2}$ (CB_2R-L185)[31,32]. We observed improved binding of [³H]CP55,940 for LEI-102 and HU308 with the CB_1R-$H270^{ECL2}L$ mutation, while the non-selective agonists showed no change (**Table 4.S3**). Through the loss of this ionic lock, selectivity over CB_1R is partially lost, showing that expulsion of ECL2 upon ligand entry may play an important role in selectivity.

In recent years, computational studies have suggested that lipophilic ligands for various GPCRs, such as the opsin receptor, sphingosine-1-phosphate receptor 1 (S1P$_1$) and cannabinoid receptors, might gain access to the binding pocket through lateral diffusion via a membrane channel between TM1 and TM7[32,41,48–51]. We experimentally examined this membrane entry pathway by creating a CB$_2$R quadruple mutant (K33$^{1.32}$Q, V36$^{1.35}$I, C40$^{1.39}$S and K279$^{7.33'}$T) for which we observed a significant loss of potency and a corresponding trend in reduced affinity, although not significant, for HU308 and the endocannabinoids (**Figure 4.4e-j**, **Table 4.S6**, **4.S7**). These compounds are more lipophilic than LEI-102 and APD371, making them more suitable to traverse the membrane to enter between TM1 and TM7. Notably, HU308 and anandamide also showed a substantially longer ET in our assays compared to the other agonists (**Table 4.S2**). This might suggest a possible relationship between a slower association and membrane channel entry at the CB$_2$R. Likewise, for a peptide GPCR a trend in reduced association rate was found with increasing lipophilicity[52]. Nevertheless, this is in contrast with the mechanism at the α_2-adrenoceptor at which lipophilic compounds had a faster association rate[53]. This shows the diversity in drug-target binding kinetics as receptor-specific properties and thus the importance of investigating these mechanisms for individual receptors[54].

The discovery of a membrane access channel for endocannabinoids on the CB$_2$R is also intriguing from a physiological perspective. Endocannabinoids are produced on demand and act as autocrine or paracrine effectors in the immune system regulating the migration of CB$_2$R-expressing immune cells[17]. Our results suggest that endocannabinoids first have to travel through the plasma membrane via lateral diffusion to reach the receptor. This may suggest that the trafficking and cellular uptake of endocannabinoids could be regulated through extracellular or intracellular vesicles that merge with the plasma membrane. Regardless of the exact mechanism of endocannabinoid trafficking, this study provides experimental evidence of a membrane channel located between TM1 and TM7 in CB$_2$R that is being used by the endocannabinoids to enter the receptor.

The ligands of the CB$_2$R, such as the phytocannabinoids and endocannabinoids, are typically very lipophilic, which comes at a cost of reduced solubility, increased off-target activity and poor pharmacokinetic properties[10,25]. Thus, balancing lipophilicity of a drug candidate is an important goal in medicinal chemistry. The first generation of experimental drugs targeting the CB$_2$R mimicked the plant-based cannabinoids. Consequently, they were highly lipophilic and suffered from poor clinical translation[10]. New generations of CB$_2$R agonists have optimized physico-chemical properties. For instance, LEI-102 and APD371 are orders of magnitude more hydrophilic than HU308. Remarkably, they can bind the same binding pocket in CB$_2$R as HU308. Our data revealed that LEI-102 and APD371 do not enter the receptor via the membrane channel like HU308, but gain access most likely via the extracellular space. LEI-102 and APD371 also form a specific (indirect) polar interaction network with H95$^{2.65}$ to activate CB$_2$R, which is not observed for HU308. This flexibility of the CB$_2$R binding pocket to be activated by a diverse set of chemotypes allows to select for a chemotype with more drug-like properties. This notion is supported by the oral efficacy of LEI-102 in the chemotherapy-induced nephropathy model and lack of CNS-adverse side effects (**Figure 4.5**, **4.6**).

Targeting CB_2R with agonists is a promising avenue for the treatment of autoimmune diseases, neuroinflammation and various forms of tissue injury/inflammation/fibrosis in the liver, heart, brain, and kidney[17]. In this study we show that LEI-102 protects against cisplatin-induced nephropathy in a CB_2R-dependent manner by attenuating kidney inflammation and injury (**Figure 4.5**). We also show that CB_2R knockout mice develop more severe nephropathy compared to their wild types suggesting protective role of endocannabinoid-CB_2R signaling during kidney injury. These results are consistent with protective effects of CB_2R agonists in various models of kidney injury/diseases and deleterious effect of CB_2R deletion in these models[29,55–63].

In conclusion, we have discovered LEI-102 as a selective CB_2R agonist that is efficacious in attenuating tissue injury in chemotherapy-induced nephropathy model without inducing CNS-mediated side effects. Using LEI-102 and five other CBR agonists we have shown that the physicochemical properties determine not only pharmacokinetic properties of ligands, but also how they engage with their target. Altogether, we elucidated several important molecular mechanisms for selective engagement and activation of the CB_2R, which may have implications for drug design and lipid signaling at GPCRs in general.

4.4 Materials and methods

4.4.1 *General materials for functional assays*

Monoclonal M2 mouse anti-FLAG primary antibody (#F3165) was purchased from Sigma-Aldrich (Zwijndrecht, the Netherlands), while secondary goat anti-mouse HRP-conjugated antibody (#115-035-003) was bought from Jackson ImmunoResearch Laboratories (West Grove, PA, USA). Bicinchoninic acid (BCA) ad BCA protein assay reagent was obtained from Pierce Chemical Company (Rockford, IL, USA). [³H]RO6957022 (specific activity 82.83 Ci mmol⁻¹) was custom synthesized at F. Hoffman-La Roche Ltd (Basel, Switzerland). [³⁵S]GTPγS (specific activity 1250 Ci mmol⁻¹ #NEG030H250UC), [³H]CP55,940 (specific activity 108.5 Ci mmol⁻¹ #NET1051250UC) and GF/C filter plates (#6055690) were purchased from Revvity (Waltham, MA, USA). CP55,940 (#C1112), AM630 (#SML0327) and DL-dithiothreitol (DTT, #646563) were obtained from Sigma-Aldrich, HU308 (#H800010) was from LKT Laboratories (St. Paul, MN, USA), APD371 was provided by F. Hoffmann-La Roche Ltd, anandamide (AEA, #1339), 2-Arachidonylglycerol (2-AG, #1298) and phenylmethylsulfonyl fluoride (PMSF, #4486) were purchased from Tocris Bioscience (Bristol, UK) and GDP (#J61646) was from Thermo Fisher Scientific (Waltham, MA, USA). All buffers and solutions were prepared using Millipore water (deionized using a MilliQ A10 Biocel with a 0.22 μm filter) and analytical grade reagents and solvents. Buffers are prepared at room temperature (rt) and stored at 4 °C, unless stated otherwise.

4.4.2 *Cell lines*

Spodoptera frugiperda (*Sf*9) cells were used for CB_2R-G_i co-expression for cryo-EM studies. *Sf*9 cells were grown in ESF 921 medium (Expression systems) at 27 °C and 125 rpm.

For transfections, human embryonic kidney 293 T (HEK293T; female, ATCC #CRL-3216) cells were grown as monolayers in culture medium i.e. Dulbecco's Modified Eagle's Medium (Sigma-Aldrich #6546), supplemented with 10% fetal calf serum (Sigma-Aldrich #F7524), 2 mM L-glutamine (Sigma-Aldrich #G8541), 100 IU/mL penicillin and 100 μg/mL streptomycin (Duchefa Biochemie #P0142 and #S0148) under a humidified atmosphere at 37 °C with 5% CO$_2$. Subculture was done twice a week at 80 - 90% confluence on 10 cm ø plates by trypsinization. CHO cells stably expressing hCB$_2$R (CHOK1_hCB$_2$bgal; PathHunter EA Parental Cell line, female, DiscoverX #93-0706C2) or hCB$_1$R (CHOK1_hCB$_1$bgal; PathHunter EA Parental Cell line, female, DiscoverX #93-0959C2) were cultured in Ham's F12 Nutrient Mixture (Sigma-Aldrich #4888) supplemented with 10% fetal calf serum, 2 mM L-glutamine, 100 IU/mL penicillin, 100 μg/mL streptomycin, 300 μg/mL hygromycin (Bio-Connect #ANT-HG-5) and 800 μg/mL G418 (Bio-Connect #SC-29065B) in a humidified atmosphere at 37 °C with 5% CO$_2$. Cells were subcultured twice a week when reaching 80 - 90% confluence on 10 or 15 cm ø plates by trypsinization.

4.4.3   *Synthesis of LEI-102 (***Figure 4.S1***)*

All reagents and solvents were purchased from commercial sources and were of analytical grade (Sigma-Aldrich, BroadPharm®). Reagents and solvents were not further purified before use. All moisture sensitive reactions were performed under inert atmosphere. Solvents were dried using 4 Å molecular sieves prior to use when anhydrous conditions were required. Water used in reactions was always demineralized. Analytical Thin-layer Chromatography (TLC) was routinely performed to monitor the progression of a reaction and was conducted on Merck Silica gel 60 F254 plates. Reaction compounds on the TLC plates were visualized by UV irradiation (λ_{254}) and/or spraying with potassium permanganate solution (K$_2$CO$_3$ (40 g), KMnO$_4$ (6 g), and H$_2$O (600 mL)), ninhydrin solution (ninhydrin (1.5 g), n-butanol (100 mL) and acetic acid (3.0 mL)) or molybdenum solution ((NH$_4$)$_6$MO$_7$·4H$_2$O (25 g/L) and (NH$_4$)$_4$Ce(SO$_4$)4·H$_2$O (10 g/L) in sulfuric acid (10%)) followed by heating as appropriate. Purification by flash column chromatography was performed using Screening Devices B.V. silica gel 60 (40-63 μm, pore diameter of 60 Å). Solutions were concentrated using a Heidolph laborata W8 4000 efficient rotary evaporator with a Laboport vacuum pump.

Analytical purity was determined with Liquid Chromatography-Mass Spectrometry (LC-MS) using a Finnigan LCQ Advantage MAX apparatus with electrospray ionization (ESI), equipped with a Phenomenex Gemini 3 μm NX-C18 110Å column (50x4.6mm), measuring absorbance at 254 nm using a Waters 2998 PDA UV detector and the m/z ratio by using an Acquity Single Quad (Q1) detector. Injection was with the Finnigan Surveyor Autosampler Plus and pumped through the column with the Finnigan Surveyor LC pump plus to be analyzed with the Finnigan Surveyor PDA plus detector. Samples were analyzed using eluent gradient 10% → 90% ACN in MilliQ water (+ 0.1% TFA (v/v)).

For purification by mass guided preparative High-Performance Liquid Chromatography (Prep-HPLC) the Waters AutoPurification HPLC/MS apparatus was used with a Gemini prep column 5 μm 18C 110 Å (150x21.2mm), Waters 2767 Sample manager, Waters 2545 Binary gradient module, Waters SFO System fluidics organizer, Waters 515 HPLC pump M,

Waters 515 HPLC pump L attached to a Waters SQ detector Acquity Ultra performance LC.

^{1}H, ^{13}C, ^{1}H-COSY and HSQC Nuclear Magnetic Resonance (NMR) spectra were recorded on a Bruker AV 300 (300/75 MHz), AV 400 (400/100 MHz) or AV 500 (500/125 MHz) spectrometer at ambient temperature using CDCl$_3$ as solvent. Chemical shifts (δ) are referenced in parts per million (ppm) with tetramethylsilane (TMS) or CDCl$_3$ resonance as the internal standard peak (CDCl$_3$/TMS, δ 0.00 for ^{1}H (TMS), δ 77.16 for ^{13}C (CDCl$_3$)). Multiplicity is reported as s = singlet, d = doublet, dd = doublet of doublet, t = triplet, q = quartet, p = quintet, m = multiplet. Coupling-constants (*J*) are reported in Hertz (Hz).

(6-bromo-3-fluoropyridin-2-yl)methanol (2): To a solution of 6-bromo-3-fluoro-2-methylpyridine **(1**, 10.7 g, 56.3 mmol, 1 eq)** under an inert atmosphere at 0 °C in DCM (370 mL) was added portion-wise *m*-CPBA (23.6 g, 70-75%, 100 mmol, 1.8 eq). The reaction mixture was stirred at room temperature (rt) for 4 days. Sat. NaHCO$_3$ and sat. Na$_2$S$_2$O$_3$ was added (1:1, v/v) and the layers were separated. The aqueous layer was extracted thrice with DCM. The combined organic layer was dried over MgSO$_4$, filtered, and concentrated under reduced pressure. To the residue was added TFAA (17 mL, 122 mmol, 2.2 eq) at 0 °C. After 15 minutes the temperature was increased to 55 °C for 3 h. The mixture was concentrated under reduced pressure, redissolved in DCM and sat. Na$_2$CO$_3$ was added. The layers were separated and the organic layer was washed with sat. NaHCO$_3$. The solvent was evaporated and the crude was dissolved in THF:MeOH (20:1, v/v) and K$_2$CO$_3$ (18.2 g, 132 mmol, 2.3 eq) was added. After 17 h H$_2$O was added and the layers were separated. The aqueous layer was extracted thrice with EtOAc. The combined organic layers were dried over MgSO$_4$, filtered, and the solvent evaporated under reduced pressure. The crude was purified with flash column chromatography (10-20% EtOAc in pentane) to yield 5.79 g (19.7 mmol, 35%) of a white solid. ^{1}H-NMR (500 MHz, CDCl$_3$) δ 7.42 (ddt, *J* = 8.5, 3.5, 0.7 Hz, 1H), 7.29 (t, *J* = 8.5 Hz, 1H), 4.80 (d, *J* = 3.3 Hz, 2H). ^{13}CNMR (126 MHz, CDCl$_3$) δ 156.10 (d, *J* = 256.2 Hz), 148.74 (d, *J* = 19.1 Hz), 135.01 (d, *J* = 2.9 Hz), 128.17 (d, *J* = 4.2 Hz), 126.09 (d, *J* = 19.8 Hz), 59.07.

(6-bromo-3-fluoropyridin-2-yl)methyl methanesulfonate (3): To a cooled (0 °C) mixture of (6-bromo-3-fluoropyridin-2-yl)methanol (1.6 g, 7.8 mmol, 1 eq) and Et$_3$N (2.5 mL, 17.9 mmol, 2.3 eq) in dry THF (40 mL) was added dropwise MsCl (1.0 mL, 12.9 mmol, 1.7 eq). After stirring at rt for 1 h the solution was concentrated under reduced pressure. DCM and H$_2$O were added and the layers were separated. The aqueous layer was extracted thrice with DCM. The combined organic layers were washed with brine, dried over MgSO$_4$, filtered, and the solvent evaporated under reduced pressure to yield 1.65 g (5.8 mmol, 75%) of an yellow solid. ^{1}H-NMR (500 MHz, CDCl$_3$) δ 7.52 (dd, *J* = 8.6, 3.5 Hz, 1H), 7.37 (t, *J* = 8.5 Hz, 1H), 5.33 (d, *J* = 2.1 Hz, 2H), 3.13 (s, 3H). ^{13}C-NMR (126 MHz, CDCl$_3$) δ 157.82 (d, *J* = 261.3 Hz), 142.15 (d, *J* = 16.0 Hz), 130.74 (d, *J* = 4.4 Hz), 127.06 (d, *J* = 20.4 Hz), 65.50 (d, *J* = 1.6 Hz), 38.39.

***N*-((6-bromo-3-fluoropyridin-2-yl)methyl)tetrahydro-2*H*-pyran-4-amine** **(4)**: (6-Bromo-3-fluoropyridin-2-yl)methyl methanesulfonate (1.49 g, 5.3 mmol, 1 eq), K$_2$CO$_3$ (1.6 g, 11.6 mmol, 2.2 eq) and tetrahydro-2*H*-pyran-4-amine (0.66 mL, 6.7 mmol, 1.3 eq) were suspended in acetonitrile and stirred at 50 °C for 6 h, then an additional 3 days at

rt. After dilution with DCM and H$_2$O the layers were separated. The aqueous layer was extracted thrice with DCM. The combined organic layers were dried over MgSO$_4$, filtered, and the solution evaporated under reduced pressure. The crude was purified with flash column chromatography (20-100% EtOAc in pentane) to yield 1.01 g (3.5 mmol, 67%) as a yellow oil. ^{1}H-NMR (300 MHz, CDCl$_3$) δ 7.40 (dd, J = 8.6, 3.6 Hz, 1H), 7.35 – 7.26 (m, 1H), 4.08 – 3.95 (m, 4H), 3.42 (td, J = 11.6, 2.2 Hz, 2H), 2.74 (tt, J = 10.5, 4.1 Hz 1H), 1.89 (ddd, J = 12.7, 4.5, 2.3 Hz, 2H), 1.52 (dtd, J = 13.1, 11.0, 4.5 Hz, 2H). ^{13}C-NMR (75 MHz, CDCl$_3$) δ 157.12 (d, J = 255.9 Hz), 149.21 (d, J = 17.0 Hz), 127.83 (d, J = 4.2 Hz), 125.97 (d, J = 21.2 Hz), 66.76, 53.64, 44.90, 33.59.

2-((4-bromobenzyl)amino)acetamide (6): To a mixture of 4-bromobenzaldehyde **(5**, 9.2 g (49.7 mmol, 1.1 eq**)** and 2-aminoacetamide hydrochloride (5.06 g, 45.8 mmol, 1.0 eq) in MeOH:H$_2$O (170 mL, 5:1, v/v) was added NaOH (2.06 g, 51.5 mmol, 1.1 eq) and left to stir at rt overnight. NaBH$_4$ (3.6 g, 95.2 mmol, 2.1 eq) was added and the solution was stirred overnight at rt. The solution was acidified to pH 3 with 2 M HCl, then neutralized with sat. aqueous NaHCO$_3$. Methanol was evaporated under reduced pressure and the resulting slurry was filtered to yield 11.0 g (45.2 mmol, 91%) of a white solid. ^{1}H-NMR (300 MHz, methanol-d$_4$) δ 7.69 – 7.59 (m, 2H), 7.47 – 7.38 (m, 2H), 4.22 (s, 2H), 3.81 (s, 2H).

1-(4-bromobenzyl)imidazolidine-2,4-dione (7): To a suspension of 2-((4-bromobenzyl)-amino)acetamide (10.0 g, 40.1 mmol, 1,0 eq) in acetonitrile (300 mL) were added CDI (13.86 g, 85.5 mmol, 2.1 eq) and DMAP (10.2 g, 83.5 mmol, 2.1 eq). The mixture was heated to 60 °C under inert atmosphere for 70 h. HCl (1 M, 250 mL) was added and the aqueous layer extracted thrice with EtOAc. The combined organic layers were washed with H$_2$O and brine, dried over MgSO$_4$, filtered, and the solvent evaporated under reduced pressure. The crude was purified with flash column chromatography with dry loading over Celite (5-10% acetone in DCM) to yield 3.95 g (14.7 mmol, 37%) of a yellow solid. ^{1}H-NMR (300 MHz, CDCl$_3$) δ 7.83 (bs, 1H), 7.56 – 7.45 (m, 2H), 7.20 – 7.10 (m, 2H), 4.49 (s, 2H), 3.79 (s, 2H). ^{13}C-NMR (75 MHz, CDCl$_3$) δ 132.41, 129.95, 77.58, 77.16, 76.74, 50.36, 46.01.

1-(4-bromobenzyl)-3-isobutylimidazolidine-2,4-dione   (8):   To   solution   of 1-(4-bromobenzyl)imidazolidine-2,4-dione (2.00 g, 7.4 mmol, 1,0 eq) in anhydrous DMF (18 mL) were subsequently added K$_2$CO$_3$ (3.08 g, 22.3 mmol, 3,0 eq) and 1-bromo-2-methylpropane (1.62 mL, 14.9 mmol, 2,0 eq) and the mixture was stirred for 20 h at rt. The mixture was filtered and the filtrate diluted with diethyl ether and washed thrice with water (3 x 50 mL). The combined organic layers were washed with brine, dried (MgSO$_4$), filtered, and concentrated under reduced pressure. The crude was purified with flash column chromatography (10-40% EtOAc in pentane) to yield 2.12 g (6.52 mmol, 88%) of a white solid. LCMS (LCQ Fleet, 10 90%): t$_r$ = 7.00 min, m/z: 325.17 [M+H]$^+$, 327.08 [M+H]$^+$ (Br). ^{1}HNMR (300 MHz, CDCl$_3$) δ 7.47 (d, J = 8.3 Hz, 2H), 7.14 (d, J = 8.3 Hz, 2H), 4.52 (s, 2H), 3.74 (s, 2H), 3.33 (d, J = 7.4 Hz, 2H), 2.15 – 2.04 (m, 1H), 0.91 (d, J = 6.8 Hz, 6H). ^{13}C NMR (75 MHz, CDCl$_3$) δ 169.57, 156.78, 134.41, 131.79, 129.48, 121.77, 60.01, 48.61, 45.98, 45.71, 28.57, 19.70.

3-isobutyl-1-(4-(4,4,5,5-tetramethyl-1,3,2-dioxaborolan-2-yl)benzyl)imidazolidine-2,4-dione (9): A mixture of 1-(4-bromobenzyl)-3-isobutylimidazolidine-2,4-dione (0.50 g,

1.54 mmol, 1 eq), KOAc (0.66 g, 6.76 mmol, 4.4 eq) and bis(pinacolato)diboron (0.59 g, 2.31 mmol, 1.5 eq) in DMF (10 mL) was sonicated for 15 min under argon flow. Subsequently, Pd(dppf)Cl$_2$ (0.07 g, 0.09 mmol, 0.06 eq) was added and the mixture was stirred at 75 °C for 20 h. The mixture was cooled to rt, diluted with EtOAc (100 mL) and water (10 mL) and the layers were separated. The water layer was extracted thrice with EtOAc (3 × 20 mL). The combined organic layers were extracted with sat. aqueous NaHCO$_3$, water and brine, dried (MgSO$_4$), filtered, and concentrated under reduced pressure. The raw product was co-evaporated with CHCl$_3$ and used in the next step without further purification.

1-(4-(5-fluoro-6-((((tetrahydro-2*H*-pyran-4-yl)amino)methyl)pyridin-2-yl)benzyl)-3-isobutylimidazolidine-2,4-dione (LEI-102): To a degassed mixture of *N*-((6-bromo-3-fluoropyridin-2-yl)methyl)tetrahydro-2*H*-pyran-4-amine (**4**, 0.29 g, 1.0 mmol, 1,0 eq), 3-isobutyl-1-(4-(4,4,5,5-tetramethyl-1,3,2-dioxaborolan-2-yl)benzyl)imidazolidine-2,4-dione (**9**, 0.56 g, ~1.5 mmol, crude) and K$_2$CO$_3$ (1.29 g, 6.0 mmol, 6,0 eq) in toluene:ethanol (10 mL, 4:1, v/v) was added under argon atmosphere Pd(PPh$_3$)$_4$ (0.18 g, 0.10 mmol, 0.1 eq) . The resulting mixture was stirred for 18 h at 75 °C, subsequently cooled to rt and filtered. The filtrate was diluted with EtOAc and washed with water and brine, dried (MgSO$_4$), filtered, and concentrated under reduced pressure. The crude was purified with flash column chromatography (0-20% MeOH in EtOAc) to yield 0.24 g of a white solid (0.53 mmol, 53%). Further purification with preparative HPLC resulted in a yield of 0.204 g (0.45 mmol, 45%). LCMS (LCQ Advantage, 10 90%): t$_r$ = 5.32 min, m/z: 455.27 [M+H]$^+$, 908.93 [2M+H]$^+$. HRMS (ESI+) m/z: calcd. for C$_{25}$H$_{32}$FN$_4$O$_3$ [M+H], 455.245; found, 455.245. ^{1}H NMR (400 MHz, CD$_3$CN) δ 8.05 (d, *J* = 8.3 Hz, 2H), 7.86 (dd, *J* = 8.7, 3.6 Hz, 1H), 7.61 (t, *J* = 9.0 Hz, 1H), 7.34 (d, *J* = 8.1 Hz, 2H), 4.53 (s, 2H), 4.45 (s, 2H), 3.93 (dd, J = 11.4, 4.4 Hz, 2H), 3.77 (s, 1H), 3.47 (tt, *J* = 11.8, 3.8 Hz, 2H), 3.30 (td, *J* = 11.9, 1.9 Hz, 2H), 3.24 (d, *J* = 7.3 Hz, 2H), 2.05 (br d, *J* = 13.3 Hz, 2H), 1.99 (dt, *J* = 13.2, 6.6 Hz, 1H), 1.83 (qd, *J* = 12.1, 4.5 Hz, 2H), 0.88 (d, *J* = 6.7 Hz, 6H). ^{13}C NMR (100 MHz, CD$_3$CN) δ 171.54, 157.25 (d, *J* = 226.6 Hz), 156.12, 153.03 (d, *J* = 4.5 Hz), 140.51 (d, *J* = 16.1 Hz), 138.83, 137.70, 129.13, 128.22, 125.56 (d, *J* = 18.8 Hz), 122.81 (d, *J* = 4.3 Hz), 118.38, 66.55, 55.55, 50.30, 46.81 (d, *J* = 7.9 Hz), 42.95, 30.02, 28.32, 20.32.

4.4.4   Constructs

The N-BRIL fused wild type (WT) human CB$_2$R construction and co-expression of G protein for cryo-EM study were performed using the similar procedure as described before[34]. In brief, the WT human CB$_2$R was modified to contain a fusion protein BRIL to improve the protein expression and thermostability, along with a 10×His-tag and a FLAG-tag at the N-terminal. The CB$_2$R, Gα$_{i1}$ and Gβ$_1$γ$_2$ subunits were cloned into the pFastBac vector separately using cloning kits.

4.4.5   Expression and purification of CB$_2$R-G$_i$-Scfv16 complexes

Methods of complex expression and purification in the current study have been described previously[34]. The CB$_2$R and G$_i$ heterotrimer were co-expressed in *Sf*9 insect cells using

the Bac-to-Bac Baculovirus Expression System (Invitrogen). Cells were infected with three separate virus preparations for CB$_2$R, Ga_{i1} and G$\beta_1\gamma_2$ at a ratio of 1:2:2 at a cell density of 2.5×10^6 cells/mL. After 48 h, the cell culture was collected by centrifugation and the cell pellets were stored at -80 °C until use. The cell pellets were thawed and lysed in the hypotonic buffer of 10 mM HEPES (pH 7.5), 10 mM MgCl$_2$, 20 mM KCl with EDTA-free complete protease inhibitor cocktail tablets (Roche, #5056489001). The CB$_2$R-G$_i$ complex was formed in membranes by addition of 25 µM agonist (LEI-102, APD371, HU308 and CP55,940, respectively) and 2 units of apyrase (NEB, #M0398S) in the presence 500 µg scFv16. The lysate was incubated for overnight at 4 °C and discard the supernatant by centrifugation at 186,000 × g for 30 min. Subsequently, the solubilization buffer containing 50 mM HEPES (pH 7.5), 100 mM NaCl, 0.75% (w/v) lauryl maltose neopentyl glycol (LMNG, Anatrace, #4216588), 0.15% (w/v) cholesterol hemisucinate (CHS, Sigma-Aldrich, #C6512) supplemented with 25 µM agonist and 2 units of apyrase (NEB) were added to solubilize complexes for 2 h at 4 °C. Insoluble material was removed by centrifugation at 186,000 × g for 30 min and the supernatant was immobilized by batch binding to TALON IMAC resin (Clontech, #635507) including 20 mM imidazole over 6 h at 4 °C. Then, the resin was packed and washed with 15 column volumes (CVs) of washing buffer I containing 25 mM HEPES (pH 7.5), 100 mM NaCl, 10% (v/v) glycerol, 0.1% (w/v) LMNG, 0.02% (w/v) CHS, 30 mM imidazole and 20 µM agonist, and 15 CVs of washing buffer II containing 25 mM HEPES (pH 7.5), 100 mM NaCl, 10% (v/v) glycerol, 0.03% (w/v) LMNG, 0.006% (w/v) CHS, 50 mM imidazole and 20 µM agonist. After that, the protein was eluted using 3 CVs of elution buffer containing 25 mM HEPES (pH 7.5), 100 mM NaCl, 10% (v/v) glycerol, 0.01% (w/v) LMNG, 0.002% (w/v) CHS, 250 mM imidazole and 25 µM agonist. Finally, the complex was concentrated using the centrifugal filter with 100 KD molecular weight cutoff and loaded onto a Superdex200 10/300 GL column (GE Healthcare) with buffer containing 20 mM HEPES (pH 7.5), 100 mM NaCl, 0.00075% (w/v) LMNG, 0.00025% GDN (Anatrace, #GDN101), 0.0001% (w/v) CHS, 100 µM TCEP. The fractions consisting of purified CB$_2$R-G$_i$ complex were collected and concentrated to 0.8-1.0 mg/ml for electron microscopy experiments.

4.4.6 *Cryo-EM grid preparation and data collection*

For cryo-EM grids preparation of the CB$_2$R-G$_i$ complexes, 3 µL of the concentrated protein was loaded to a glow-discharged holey carbon grid (CryoMatrix Amorphous alloy film R1.2/1.3, 300 mesh), and subsequently were plunge-frozen in liquid ethane using a Vitrobot Mark IV (Thermo Fisher Scientific). The chamber of Vitrobot was set to 100% humidity at 4 °C. The sample was blotted for 2.5 s with blot force 2. Cryo-EM images were collected on a Titan Krios microscope operated at 300 kV equipped with a Gatan Quantum energy filter, with a slit width of 20 eV, a Gatan K2 summit direct electron camera (Gatan). Images were taken at a dose rate of 8e$^-$/Å^2/s with a defocus range of -0.8 to -2.0 µm using SerialEM software[64] in EFTEM nanoprobe mode, with 50 µm C2 aperture, at a calibrated magnification of 130,000 corresponding to a magnified pixel size of 1.04 Å. The total exposure time was 8.1 s and 45 frames were recorded per micrograph.

4.4.7   Cryo-EM image processing

The cryo-EM data processing was performed with CryoSPARC[65]. For CB_2R-$G\alpha_i$-scFv16-APD371/LEI-102/HU308/CP55,940 dataset, a total of 7443, 5282, 7530 and 6473 movies were collected, respectively. For all datasets, patch motion correction was used for beam-induced motion correction. Contrast transfer function (CTF) parameters for each micrograph were determined by patch CTF estimation. Using Blob Picker in CryoSPARC to auto pick particles in the first 500 micrographs of CB_2R-$G\alpha_i$-scFv16-APD371 complex dataset and then 258347 particles were extracted to conduct 2D classification. 9277 particles in good 2D patterns were selected as templates to pick better particles. 5,239,870, 3,398,611, 4,653,294 and 3,595,875 particles extracted, respectively, in a 256 Å box were divided into three hundred two-dimensional (2D) class averages with a maximum alignment resolution of 6 Å. Then, 1,152,146, 762,471, 355,832 and 440,292 particles were selected from good 2D classification after two round 2D classification, individually. Following 2D classification, these particles were subjected for ab initio reconstruction into four classes. After heterogeneous refinement, homogeneous refinement, non-uniform refinement and local refinement of the best-looking dataset in CryoSPARC, the final map has an indicated global resolution of 3.08 Å, 2.98 Å, 2.97 Å and 2.84 Å at a Fourier shell correlation (FSC) of 0.143, respectively. Local resolution was determined using the Bsoft package with half maps as input maps[66].

4.4.8   Model building and refinement

For CB_2R-G_i-scFv16 complex, the CB_2R-AM12033 cryo-EM structure and G_i protein in CB_2R were used as the starting model. The model was docked into the EM density map using Chimera[67], followed by iterative manual adjustment and rebuilding in COOT[68] and phenix.real_space_refine in Phenix[69]. The model statistics were validates using MolProbity[70]. Structural figures were prepared in Chimera and PyMOL (http://www.pymol.org). The final refinement statistics are provided in **Table 4.S4**. The extent of any model overfitting during refinement was measured by refining the final model against one of the half-maps and by comparing the resulting map versus model FSC curves with the two half-maps and full model.

4.4.9   Generation of mutants

The WT CB_1R and CB_2R genes were subcloned into vector pcDNA3.1 with an N-terminal HA signal peptide and FLAG-tag. Mutations were introduced by QuikChange PCR (as described by supplier).

4.4.10   Transfection

24 h prior to transfection, HEK293T cells were seeded on 10 cm ø plates to reach approximately 50% confluence at the start of transfection. The cells were transfected

with 10 µg plasmid DNA of WT hCB$_2$R or hCB$_1$R receptor, or mutant receptor using the calcium phosphate precipitation method[71]. In short, a DNA-calcium mix was made containing 270 mM CaCl$_2$ and 10 µg plasmid DNA to which Hank's Balanced Salt Solution (HBSS; 280 mM NaCl, 10 mM KCl, 1.5 mM Na$_2$HPO$_4$ and 50 mM HEPES) was added in a 1:1 (v/v) ratio and mixed by aeration to create consistent calcium phosphate precipitates. For transfection, 1 mL DNA-calcium mix was added per 10 cm ø plate, followed by a 48 h incubation under a humidified atmosphere at 37 °C with 5% CO$_2$.

4.4.11   Enzyme-linked immunosorbent assay (ELISA)

Receptor expression after transfection was measured in an enzyme-linked immunosorbent assay (ELISA). After 24 h of transfection, HEK293T cells were detached with phosphate-buffered saline (PBS)/EDTA and seeded into a sterile 96-well poly-D-lysine coated plate at a density of 100,000 cells per well and kept under a humidified atmosphere at 37 °C with 5% CO$_2$. After an additional 24 h, cells were washed with PBS and fixed with 4% formaldehyde for 10 min at RT. Cells were washed twice with Tris-buffered saline (TBS) and were blocked with TBS supplemented with 0.1% TWEEN 20 (TBST) and 2% BSA (w/v)) for 30 min at rt while shaking. Subsequently, the cells were incubated with monoclonal M2 mouse anti-FLAG primary antibody (1:4000) for 2 h at rt while shaking. After removal of the antibody, the cells were washed three times with TBST and incubated with the secondary goat anti-mouse HRP-conjugated antibody (1:10,000) for 1 h at rt while shaking. After a final wash with TBS, the cells were treated with 3,3',5,5'-Tetramethylbenzidine (TMB, Sigma-Aldrich #T0440) in the dark for maximally 10 min at rt to visualize immunoreactivity. The reaction was quenched with 1 M H$_3$PO$_4$, and absorbance was read at 450 nm with a Wallac EnVision 2104 Multilabel reader (Revvity).

4.4.12   Membrane preparation

For membrane preparation, HEK293T cells were harvested 48 h after transfection. Cells were detached by scraping into 3 mL of PBS and subsequently centrifuged at 2000 × g for 5 min. Pellets were resuspended in ice-cold Tris buffer (50 mM Tris-HCl, pH 7.4) and homogenized with an Ultra Turrax homogenizer (IKA-Werke GmbH & Co. KG, Staufen, Germany). Cytosolic and membrane fractions were separated using a high-speed centrifugation step of 31,000 rpm in a Beckman Optima LE-80K ultracentrifuge with Ti70 Rotor for 20 min at 4 °C. After a second cycle of homogenization and centrifugation, the final pellets were resuspended in 50 mM Tris-HCl pH 7.4, 5 mM MgCl$_2$ and stored in 100 µL aliquots at -80 °C until use. CHOK1_hCB$_2$bgal and CHOK1_hCB$_1$bgal cells were harvested when reaching 90% confluence in 15 cm ø plates after one week subculture at a 1:6 ratio. Membrane preparation followed a similar procedure as described above. Final membrane pellets were resuspended in 50 mM Tris-HCl pH 7.4 and stored in 100 µL aliquots at -80 °C until use. Membrane protein concentrations were determined using a BCA protein determination assay as described by the manufacturer[72].

4.4.13   *[³H]RO6957022 competition association assays*

For assessment of kinetic agonist binding at hCB$_2$R, [³H]RO6957022 competition association assays were executed. These assays were previously described with the main difference of incubation at 25 °C compared to 10 °C for identification of more distinct kinetic differences[73]. In short, prior to kinetic assessment of agonist binding, the affinity (IC$_{50}$) of the agonists at the hCB$_2$R was determined in [³H]RO6957022 displacement assays. CHOK1_hCB$_2$bgal were thawed, homogenized, and subsequently diluted to 1 µg protein per well. When studying endocannabinoids, membranes were preincubated with 50 µM PMSF for 30 min. Membranes were incubated with ~1.5 nM [³H]RO6957022 and six increasing concentrations of competing agonists in a total volume of 100 µL assay buffer (50 mM Tris-HCl (pH 7.4), 0.1% (w/v) BSA). Incubations were done for 2 h at 10 °C to reach equilibrium. Subsequently, in competition association assays, agonists were incubated at their IC$_{50}$ concentration in the presence of ~1.5 nM [³H]RO6957022 in a total volume of 100 µL assay buffer at 10 °C. Competition was initiated by addition of membrane homogenates at different time points for 2 h. Nonspecific binding (NSB) was determined with 10 µM AM630 and organic solvent (DMSO or acetonitrile) concentrations were <1% in all samples. Total radioligand binding (TB) did not exceed 10% of the amount added to prevent ligand depletion. Incubations were terminated by rapid vacuum filtration with ice-cold 50 mM Tris-HCl (pH 7.4), 0.1% (w/v) BSA buffer through Whatman GF/C filters using a Filtermate 96-well harvester (Revvity). Filters were dried for at least 30 min at 55 °C and subsequently 25 µL MicroScint scintillation cocktail (Revvity #6013621) was added per well. Filter-bound radioactivity was measured by scintillation spectrometry using a Microbeta² 2450 counter (Revvity).

4.4.14   *[³⁵S]GTPγS binding assays*

G protein activation by agonists LEI-102, APD371, HU308, CP55,940 AEA and 2-AG was measured by binding of radiolabeled [³⁵S]GTPγS to the cannabinoid receptors as previously described[25]. In short, transient HEK293T membrane homogenates (10 µg/well) were diluted in assay buffer (50 mM Tris-HCl (pH 7.4), 5 mM MgCl$_2$, 150 mM NaCl, 1 mM EDTA, 0.05% BSA (w/v) and 1 mM DTT, freshly prepared every day) and were pretreated with 10 µg saponin and 1 µM GDP. For endocannabinoid samples, the membranes were additionally pretreated for 30 minutes with 50 µM PMSF before agonist addition. To determine the G protein activation, the membranes were incubated with 10 µM or six increasing concentrations of agonist (ranging from 0.01 nM to 1 µM) for 30 minutes at rt. Basal receptor activity was determined in the presence of vehicle only (0.2% DMSO/acetonitrile). [³⁵S]GTPγS (0.3 nM) was added and the mixture was co-incubated for an additional 90 minutes at 25 °C while shaking at 400 rpm. Filtration was performed and filter-bound radioactivity was determined as described in section **4.4.13 [³H]RO6957022 competition association assays** except for using ice-cold 50 mM Tris-HCl (pH 7.4), 5 mM MgCl$_2$ buffer.

4.4.15 *[³H]CP55,940 homologous and heterologous displacement assays*

Agonist affinity (K$_i$) on WT and mutant receptors was determined in [³H]CP55,940 displacement assays. The amount of transient HEK293T membrane, ranging from 0.75 μg to 10 μg protein per well, was chosen to obtain a specific [³H]CP55,940 binding window of 1200-1500 disintegrations per minute (dpm) except for the CB$_2$R-Quadruple[TM1,7] mutant, for which a window of ~500 dpm could be obtained using 20 μg protein per well. Membranes were thawed and subsequently homogenized using the Ultra Turrax homogenizer. For the endocannabinoid assays, the membranes were preincubated for 30 min with 50 μM PMSF. Homologous displacement assays were performed with 1.5 nM final concentration [³H] CP55,940 and when necessary supplemented with an additional concentration of 0.55 nM [³H]CP55,940 in the presence of competing CP55,940 (ranging from 0.01 nM to 1 μM) in assay buffer (50 mM Tris-HCl (pH 7.4), 5 mM MgCl$_2$, 0.1% (w/v) BSA). Heterologous displacement assays were executed for LEI-102, APD371, HU308, AEA and 2-AG using 1.5 nM final concentration [³H]CP55,940 with one concentration (10 μM) or six increasing concentrations (ranging from 0.1 nM to 10 μM) in assay buffer. For both assays, binding was initiated by addition of membrane homogenates to reach a final volume of 100 μL. NSB was determined using 10 μM CP55,940 and organic solvent (DMSO or acetonitrile) concentrations were <1% in all samples. TB did not exceed 10% of the amount added to prevent ligand depletion. Incubation was done for 2 h at 25 °C to reach equilibrium. Filtration was performed and filter-bound radioactivity was determined as described in section **4.4.13 [³H]RO6957022 competition association assays** except for using ice-cold 50 mM Tris-HCl (pH 7.4), 5 mM MgCl$_2$, 0.1% (w/v) BSA buffer.

4.4.16 *Cisplatin-induced nephropathy*

Ten to twelve-week-old male/female *C57BL/6J* mice were obtained from The Jackson Laboratory (Bar Harbor, ME, USA). CB$_2$ receptor knockout mice (CB$_2$R$^{-/-}$) and their wild-type littermates (CB$_2$R$^{+/+}$) were developed as described previously and had been backcrossed to a C57BL/6J background[74]. All animals were kept in a temperature-controlled environment with a 12 h light–dark cycle and were always allowed free access to food and water.

The well-established model of cisplatin-induced nephropathy was used[63]. Mice (CB$_2$R$^{-/-}$ and CB$_2$R$^{+/+}$) were sacrificed 72 h after a single injection of cisplatin (cis-diamine platinum (II) dichloride (Sigma#P4394) 25 mg/kg i.p.; freshly dissolved in physiological saline) by cervical dislocation under deep anesthesia with 5% isoflurane, for collection of blood and tissue samples. LEI-102 was given i.p. or by oral gavage (p.o.) at 0.3, 3.0 and 10 mg/kg every day, starting 1.5 h before the cisplatin exposure. The drug was dissolved in a vehicle of DMSO:Tween 80:saline, 1:1:18. After administration of LEI‑102, mice were killed by cervical dislocation under deep anesthesia with 5% isoflurane, for collection of blood and tissue samples at the time described in the figure. All animal experiments were approved by the National Institute on Alcohol Abuse and Alcoholism Animal Care and Use Committee. The tetrad assay in mice has previously been described in detail[29].

4.4.17 Biochemistry, Histopathology, Immunostaining, Real-Time PCR

Markers of kidney dysfunction (BUN and CREA), histopathology (PAS staining), immunostaining or ELISA for 3-nitrotyrosine (3-NT; Cell Biolabs #STA-305) and 4-hydroxynonenal (4-HNE; Cell Biolabs#STA-838), and real-time PCR (Primers from Qiagen, SYBER Green Vita Scientific#MEIF01301, High-Capacity cDNA Reverse Transcription Kit, Thermo Fisher Scientific#4368813) for inflammatory cytokines were performed as previously described[63]. Tubular damage scores were determined based on the percentage of tubules showing epithelial necrosis where 0= normal; 1, < 10%; 2, 10–25%; 3, 26–75%; 4, > 75%. Tubular necrosis was defined as the loss of the proximal tubular brush border, blebbing of ff apical membranes, tubular epithelial cell detachment from the basement membrane, or intraluminal aggregation of cells and proteins. The morphometric examination was performed in a blinded manner. Ten fields were scored from each mouse kidneys at 200X magnification, and average scores were determined for each mouse. For final quantification graph, average tubular damage scores of six mice/group were plotted.

4.4.18 Quantification and statistical analysis

All experimental data were analyzed using GraphPad Prism 9.0 (GraphPad Software Inc., San Diego, CA). All values obtained are means ± standard error of the mean (SEM) of at least three independent experiments performed in duplicate, unless stated otherwise.

From [^{3}H]RO6957022 competition association assays, the k_{on} and k_{off} were determined by non-linear regression analysis, using the "kinetics of competitive binding" model as described by Motulsky and Mahan[75]:

$$K_a = k_1[L] \cdot 10^{-9} + k_2$$

$$K_b = k_3[I] \cdot 10^{-9} + k_4$$

$$S = \sqrt{(K_a - K_b)^2 + 4 \cdot k_1 \cdot k_3 \cdot [L] \cdot [I] \cdot 10^{-18}}$$

$$K_f = 0.5(K_a + K_b + S)$$

$$K_s = 0.5(K_a + K_b - S)$$

$$Q = \frac{B_{max} \cdot k_1 \cdot [L] \cdot 10^{-9}}{K_f - K_s}$$

$$[Y] = Q\left(\frac{k_4 \cdot (K_f - K_s)}{K_f \cdot K_s} + \frac{k_4 - K_f}{K_f} \cdot e^{(-K_f \cdot X)} - \frac{k_4 - K_s}{K_s} \cdot e^{(-K_s \cdot X)}\right)$$

Where [L] is the radioligand concentration per experiment (~1.5 nM), I is the IC$_{50}$ concentration of agonist (nM), X is the time (s), and Y is the specific binding of the radioligand (dpm). K_a and K_b are the observed association rate constants (k_{obs}) of the radioligand and the agonist of interest, respectively. k_1 and k_3 are the association rate constants (k_{on} in M^{-1}s^{-1}) of [^{3}H]RO6957022 (determined per experiment) and the agonist of interest, respectively. Similarly, k_2 and k_4 are the dissociation rate constants (k_{off} in s^{-1}) of [^{3}H]

Chapter 4

RO6957022 (experimentally determined at 4.3×10^{-4} s^{-1}, data not shown) and the agonist of interest, respectively. The engagement time (ET in seconds) of the agonists of interest was determined at 1 μM of agonist using the equation ET$= 1/(k_{on} \cdot 10^{-6})$. The residence time (RT in min) was calculated using the equation RT$=1/(k_{off} \cdot 60)$[76]. The association and dissociation rate constants were used to calculate the kinetic K_D using: $K_D = k_{off}/k_{on}$.

[35S]GTPγS agonist responses on hCB_2R constructs were baseline-corrected for the individual mutant's basal activity. The responses were normalized to the basal activity of the construct (0%) and top of the CP55,940 (for WT responses only) or WT curve (for mutants, 100%). The potency (pEC$_{50}$) and efficacy (E$_{max}$) values were obtained by non-linear regression to a sigmoidal concentration-effect curve with a Hill slope of 1 by using the "log(agonist) vs response (three parameters)" model. [35S]GTPγS data from hCB_1R constructs were expressed as fold over the mutant's basal activity to also quantify the effects of CB_2R selective agonists.

Displacement assays were baseline-corrected with NSB and normalized to this value (0%) and TB (100%). The equilibrium dissociation constants (K_D) of [3H]CP55,940 on different mutants were calculated from homologous displacements by non-linear regression analysis, using the "one-site homologous" model. The half-maximal inhibitory concentrations (pIC$_{50}$) of the agonists in [3H]CP55,940 and [3H]RO6957022 assays were obtained by non-linear regression analysis of the homologous and heterologous displacement curves and further converted into inhibitory constant pK$_i$ using the Cheng-Prusoff equation[77]. In which the experimentally determined K_D for each construct was used for [3H]CP55,940 assays or 0.78 nM for [3H]RO6957022 assays (data not shown).

Differences in pEC$_{50}$, E$_{max}$, pK$_D$ and pK$_i$ values for each mutant compared to WT were analyzed using a one-way Welch's ANOVA with Dunnett's T3 multiple comparisons test or an unpaired Student's t-test with Welch's correction. Significant differences are displayed as * $p < 0.05$; ** $p < 0.01$, *** $p < 0.001$ and **** $p < 0.0001$.

For the animal experiments all the values are represented as mean $\pm$ SEM. Statistical analysis of the data was performed by analysis of variance (ANOVA) followed by Tukey's post hoc test for multiple comparisons or t-test if appropriate. The analysis was conducted using GraphPad Prism 9 software. $p < 0.05$ was considered statistically significant.

4.4.19   *Data and code availability*

The atomic coordinates for CB_2R-LEI-102-G$_i$-scFv16, CB_2R-APD371-G$_i$-scFv16, CB_2R-HU308-G$_i$-scFv16 and CB_2R-CP55,940-G$_i$-scFv16 have been deposited in the Protein Data Bank with the accession codes 8GUT, 8GUQ, 8GUS and 8GUR. The EM maps for CB_2R-LEI-102-G$_i$-scFv16, CB_2R-APD371-G$_i$-scFv16, CB_2R-HU308-G$_i$-scFv16 and CB_2R-CP55,940-G$_i$-scFv16 have been deposited in EMDB with the codes EMD-34279, EMD-34276, EMD-34278 and EMD-34277, respectively.

References

1. Mechoulam, R., Hanuš, L. O., Pertwee, R. & Howlett, A. C. Early phytocannabinoid chemistry to endocannabinoids and beyond. *Nat Rev Neurosci* **15**, 757–764 (2014).

2. Pacher, P., Bátkai, S. & Kunos, G. The endocannabinoid system as an emerging target of pharmacotherapy. *Pharmacol Rev* **58**, 389–462 (2006).

3. Badowski, M. E. & Yanful, P. K. Dronabinol oral solution in the management of anorexia and weight loss in AIDS and cancer. *Ther Clin Risk Manag* **14**, 643–651 (2018).

4. Grimison, P. *et al.* Oral THC:CBD cannabis extract for refractory chemotherapy-induced nausea and vomiting: a randomised, placebo-controlled, phase II crossover trial. *Annals of Oncology* **31**, 1553–1560 (2020).

5. Inglet, S. *et al.* Clinical Data for the Use of Cannabis-Based Treatments: A Comprehensive Review of the Literature: *Annals of Pharmacotherapy* **54**, 1109–1143 (2020).

6. Jones, É. & Vlachou, S. A Critical Review of the Role of the Cannabinoid Compounds Δ^9-Tetrahydrocannabinol (Δ^9-THC) and Cannabidiol (CBD) and their Combination in Multiple Sclerosis Treatment. *Molecules* **25**, 4930 (2020).

7. Adams, I. B. & Martin, B. R. Cannabis: pharmacology and toxicology in animals and humans. *Addiction* **91**, 1585–1614 (1996).

8. Lucas, C. J., Galettis, P. & Schneider, J. The pharmacokinetics and the pharmacodynamics of cannabinoids. *Br J Clin Pharmacol* **84**, 2477–2482 (2018).

9. Pacher, P., Steffens, S., Haskó, G., Schindler, T. H. & Kunos, G. Cardiovascular effects of marijuana and synthetic cannabinoids: The good, the bad, and the ugly. *Nat Rev Cardiol* **15**, 151–166 (2018).

10. Riera, R., Pacheco, R. L., Bagattini, Â. M. & Martimbianco, A. L. C. Efficacy and safety of therapeutic use of cannabis derivatives and their synthetic analogs: Overview of systematic reviews. *Phytotherapy Research* **36**, 5–21 (2022).

11. Munro, S., Thomas, K. L. & Abu-Shaar, M. Molecular characterization of a peripheral receptor for cannabinoids. *Nature* **365**, 61–65 (1993).

12. Howlett, A. C. *et al.* International Union of Pharmacology. XXVII. Classification of cannabinoid receptors. *Pharmacol Rev* **54**, 161–202 (2002).

13. Pertwee, R. G. *et al.* International Union of Basic and Clinical Pharmacology. LXXIX. Cannabinoid Receptors and Their Ligands: Beyond CB_1 and CB_2. *Pharmacol Rev* **62**, 588–631 (2010).

14. Howlett, A. C. & Abood, M. E. CB_1 and CB_2 Receptor Pharmacology. in *Advances in Pharmacology* vol. 80 169–206 (Academic Press, 2017).

15. Howlett, A., Blume, L. & Dalton, G. CB1 Cannabinoid Receptors and their Associated Proteins. *Curr Med Chem* **17**, 1382–1393 (2010).

16. Galiègue, S. *et al.* Expression of Central and Peripheral Cannabinoid Receptors in Human Immune Tissues and Leukocyte Subpopulations. *Eur J Biochem* **232**, 54–61 (1995).

17. Pacher, P. & Mechoulam, R. Is lipid signaling through cannabinoid 2 receptors part of a protective system? *Prog Lipid Res* **50**, 193–211 (2011).

18. Hanuš, L. *et al.* HU-308: A specific agonist for CB_2, a peripheral cannabinoid receptor. *Proc Natl Acad Sci U S A* **96**, 14228–14233 (1999).

19. Guindon, J. & Hohmann, A. G. Cannabinoid CB_2 receptors: a therapeutic target for the treatment of inflammatory and neuropathic pain. *Br J Pharmacol* **153**, 319–334 (2008).

20. Hussain, M. T., Greaves, D. R. & Iqbal, A. J. The Impact of Cannabinoid Receptor 2 Deficiency on Neutrophil Recruitment and Inflammation. *DNA Cell Biol* **38**, 1025–1029 (2019).

21. Rizzo, M. D. *et al.* Targeting Cannabinoid Receptor 2 on Peripheral Leukocytes to Attenuate Inflammatory Mechanisms Implicated in HIV-Associated Neurocognitive Disorder. *Journal of Neuroimmune Pharmacology 2020 15:4* **15**, 780–793 (2020).

22. Liu, Q. R. *et al.* Anti-Inflammatory and Pro-Autophagy Effects of the Cannabinoid Receptor CB2R: Possibility of Modulation in Type 1 Diabetes. *Front Pharmacol* **12**, 809965 (2022).

23. Brennecke, B. *et al.* Cannabinoid receptor type 2 ligands: An analysis of granted patents since 2010. *Pharm Pat Anal* **10**, 111–163 (2021).

24. Whiting, Z. M., Yin, J., de la Harpe, S. M., Vernall, A. J. & Grimsey, N. L. Developing the Cannabinoid Receptor 2 (CB2) pharmacopoeia: past, present, and future. *Trends Pharmacol Sci* **43**, 754–771 (2022).

25. Soethoudt, M. *et al.* Cannabinoid CB_2 receptor ligand profiling reveals biased signalling and off-target activity. *Nat Commun* **8**, 1–14 (2017).

Chapter 4

26. Han, S. *et al.* Discovery of APD371: Identification of a Highly Potent and Selective CB$_2$ Agonist for the Treatment of Chronic Pain. *ACS Med Chem Lett* **8**, 1309–1313 (2017).

27. Yacyshyn, B. R. *et al.* Safety, Pharmacokinetics, and Efficacy of Olorinab, a Peripherally Acting, Highly Selective, Full Agonist of the Cannabinoid Receptor 2, in a Phase 2a Study of Patients with Chronic Abdominal Pain Associated with Crohn's Disease. *Crohns Colitis 360* **3**, otaa089 (2021).

28. van der Stelt, M. *et al.* Discovery and Optimization of 1-(4-(Pyridin-2-yl)benzyl)-imidazolidine-2,4-dione Derivatives As a Novel Class of Selective Cannabinoid CB2 Receptor Agonists. *J Med Chem* **54**, 7350–7362 (2011).

29. Mukhopadhyay, P. *et al.* The novel, orally available and peripherally restricted selective cannabinoid CB$_2$ receptor agonist LEI-101 prevents cisplatin-induced nephrotoxicity. *Br J Pharmacol* **173**, 446–458 (2016).

30. Soethoudt, M. *et al.* Structure-kinetic relationship studies of cannabinoid CB$_2$ receptor agonists reveal substituent-specific lipophilic effects on residence time. *Biochem Pharmacol* **152**, 129–142 (2018).

31. Hua, T. *et al.* Crystal Structure of the Human Cannabinoid Receptor CB$_1$. *Cell* **167**, 750-762.e14 (2016).

32. Shao, Z. *et al.* High-resolution crystal structure of the human CB1 cannabinoid receptor. *Nature* **540**, 602–606 (2016).

33. Li, X. *et al.* Crystal Structure of the Human Cannabinoid Receptor CB2. *Cell* **176**, 459–467 (2019).

34. Hua, T. *et al.* Activation and Signaling Mechanism Revealed by Cannabinoid Receptor-G$_i$ Complex Structures. *Cell* **180**, 655-665.e18 (2020).

35. Xing, C. *et al.* Cryo-EM Structure of the Human Cannabinoid Receptor CB2-G$_i$ Signaling Complex. *Cell* **180**, 645-654.e13 (2020).

36. Hua, T. *et al.* Crystal structures of agonist-bound human cannabinoid receptor CB$_1$. *Nature* **547**, 468–471 (2017).

37. Shao, Z. *et al.* Structure of an allosteric modulator bound to the CB1 cannabinoid receptor. *Nat Chem Biol* **15**, 1199–1205 (2019).

38. Yang, X. *et al.* Molecular mechanism of allosteric modulation for the cannabinoid receptor CB1. *Nat Chem Biol* 1–10 (2022) doi:10.1038/s41589-022-01038-y.

39. McAllister, S. D. *et al.* Structural Mimicry in Class A G Protein-coupled Receptor Rotamer Toggle Switches: the importance of the F3.36(201)/W6.48(357) interaction in cannabinoid CB$_1$ receptor activation. *Journal of Biological Chemistry* **279**, 48024–48037 (2004).

40. Díaz, Ó., Dalton, J. A. R. & Giraldo, J. Revealing the Mechanism of Agonist-Mediated Cannabinoid Receptor 1 (CB1) Activation and Phospholipid-Mediated Allosteric Modulation. *J Med Chem* **62**, 5638–5654 (2019).

41. Krishna Kumar, K. *et al.* Structure of a Signaling Cannabinoid Receptor 1-G Protein Complex. *Cell* **176**, 448–458 (2019).

42. Bow, E. W. & Rimoldi, J. M. The structure-function relationships of classical cannabinoids: CB1/CB2 modulation. *Perspect Medicin Chem* **8**, 17–39 (2016).

43. Kapur, A. *et al.* Mutation Studies of Ser7.39 and Ser2.60 in the Human CB$_1$ Cannabinoid Receptor: Evidence for a Serine-Induced Bend in CB$_1$ Transmembrane Helix 7. *Mol Pharmacol* **71**, 1512–1524 (2007).

44. Javitch, J. A., Ballesteros, J. A., Weinstein, H. & Chen, J. A Cluster of Aromatic Residues in the Sixth Membrane-Spanning Segment of the Dopamine D2 Receptor Is Accessible in the Binding-Site Crevice. *Biochemistry* **37**, 998–1006 (1998).

45. Xu, W. *et al.* Comparison of the Amino Acid Residues in the Sixth Transmembrane Domains Accessible in the Binding-Site Crevices of μ, δ, and κ Opioid Receptors. *Biochemistry* **40**, 8018–8029 (2001).

46. Wang, X. *et al.* Identification of V6.51L as a selectivity hotspot in stereoselective A$_{2B}$ adenosine receptor antagonist recognition. *Sci Rep* **11**, (2021).

47. Lin, X. *et al.* Structural basis of ligand recognition and self-activation of orphan GPR52. *Nature* **579**, 152–157 (2019).

48. Hanson, M. A. *et al.* Crystal structure of a lipid G protein-coupled receptor. *Science (1979)* **335**, 851–855 (2012).

49. Jakowiecki, J. & Filipek, S. Hydrophobic Ligand Entry and Exit Pathways of the CB1 Cannabinoid Receptor. *J Chem Inf Model* **56**, 2457–2466 (2016).

50. Stanley, N., Pardo, L. & Fabritiis, G. D. The pathway of ligand entry from the membrane bilayer to a lipid G protein-coupled receptor. *Sci Rep* **6**, 1–9 (2016).

51. Szlenk, C. T., GC, J. B. & Natesan, S. Does the Lipid Bilayer Orchestrate Access and Binding of Ligands to Transmembrane Orthosteric/Allosteric Sites of G Protein-Coupled Receptors? *Mol Pharmacol* **96**, 541 (2019).

52. Bokoch, M. P. *et al.* Entry from the Lipid Bilayer: A Possible Pathway for Inhibition of a Peptide G Protein-Coupled Receptor by a Lipophilic Small Molecule. *Biochemistry* **57**, 5748–5758 (2018).

53. Sykes, D. A. *et al.* Observed drug-receptor association rates are governed by membrane affinity: The importance of establishing 'micro-pharmacokinetic/pharmacodynamic relationships' at the β_2-adrenoceptor. *Mol Pharmacol* **85**, 608–617 (2014).

54. van der Velden, W. J. C., Heitman, L. H. & Rosenkilde, M. M. Perspective: Implications of Ligand−Receptor Binding Kinetics for Therapeutic Targeting of G Protein-Coupled Receptors. *ACS Pharmacol. Transl. Sci* **2020**, 179–189 (2020).

55. Swanson, M. L., Regner, K. R., Moore, B. M. & Park, F. Cannabinoid Type 2 Receptor Activation Reduces the Progression of Kidney Fibrosis Using a Mouse Model of Unilateral Ureteral Obstruction. *Cannabis Cannabinoid Res* **7**, 790–803 (2022).

56. Chafik, S. G., Michel, H. E. & El-Demerdash, E. The Cannabinoid-2 receptor agonist, 1-phenylisatin, protects against cisplatin-induced nephrotoxicity in mice. *Life Sci* **308**, 120928 (2022).

57. Trojnar, E. *et al.* Cannabinoid-2 receptor activation ameliorates hepatorenal syndrome. *Free Radic Biol Med* **152**, 540–550 (2020).

58. Çakır, M., Tekin, S., Doğanyiğit, Z., Çakan, P. & Kaymak, E. The protective effect of cannabinoid type 2 receptor activation on renal ischemia–reperfusion injury. *Mol Cell Biochem* **462**, 123–132 (2019).

59. Pressly, J. D. *et al.* Selective cannabinoid 2 receptor stimulation reduces tubular epithelial cell damage after renal ischemia-reperfusion injury. *Journal of Pharmacology and Experimental Therapeutics* **364**, 287–299 (2018).

60. Nettekoven, M. *et al.* Novel Triazolopyrimidine-Derived Cannabinoid Receptor 2 Agonists as Potential Treatment for Inflammatory Kidney Diseases. *ChemMedChem* **11**, 179–189 (2016).

61. Jenkin, K. A. *et al.* Renal effects of chronic pharmacological manipulation of CB2 receptors in rats with diet-induced obesity. *Br J Pharmacol* **173**, 1128–1142 (2016).

62. Barutta, F. *et al.* Deficiency of cannabinoid receptor of type 2 worsens renal functional and structural abnormalities in streptozotocin-induced diabetic mice. *Kidney Int* **86**, 979–990 (2014).

63. Mukhopadhyay, P. *et al.* Cannabinoid-2 receptor limits inflammation, oxidative/nitrosative stress and cell death in nephropathy. *Free Radic Biol Med* **48**, 467 (2010).

64. Mastronarde, D. N. Automated electron microscope tomography using robust prediction of specimen movements. *J Struct Biol* **152**, 36–51 (2005).

65. Punjani, A., Rubinstein, J. L., Fleet, D. J. & Brubaker, M. A. cryoSPARC: algorithms for rapid unsupervised cryo-EM structure determination. *Nat Methods* **14**, 290–296 (2017).

66. Heymann, J. B. Single particle reconstruction and validation using Bsoft for the map challenge. *J Struct Biol* **204**, 90–95 (2018).

67. Pettersen, E. F. *et al.* UCSF Chimera—A visualization system for exploratory research and analysis. *J Comput Chem* **25**, 1605–1612 (2004).

68. Emsley, P., Lohkamp, B., Scott, W. G. & Cowtan, K. Features and development of Coot. *Acta Crystallogr D Biol Crystallogr* **66**, 486–501 (2010).

69. Adams, P. D. *et al.* PHENIX: A comprehensive Python-based system for macromolecular structure solution. *Acta Crystallogr D Biol Crystallogr* **66**, 213–221 (2010).

70. Chen, V. B. *et al.* MolProbity: all-atom structure validation for macromolecular crystallography. *Acta Crystallogr D Biol Crystallogr* **66**, 12–21 (2010).

71. Chen, C. & Okayama, H. High-efficiency transformation of mammalian cells by plasmid DNA. *Mol Cell Biol* **7**, 2745–2752 (1987).

72. Smith, P. K. *et al.* Measurement of protein using bicinchoninic acid. *Anal Biochem* **150**, 76–85 (1985).

73. Martella, A. *et al.* A Novel Selective Inverse Agonist of the CB_2 Receptor as a Radiolabeled Tool Compound for Kinetic Binding Studies. *Mol Pharmacol* **92**, 389–400 (2017).

74. Batkai, S. *et al.* Cannabinoid-2 receptor mediates protection against hepatic ischemia/reperfusion injury. *The FASEB Journal* **21**, 1788–1800 (2007).

75. Motulsky, H. J. & Mahan, L. C. The kinetics of competitive radioligand binding predicted by the law of mass action. *Mol Pharmacol* **25**, 1–9 (1984).

Chapter 4

76. Copeland, R. A., Pompliano, D. L. & Meek, T. D. Drug–target residence time and its implications for lead optimization. *Nat Rev Drug Discov* **5**, 730–739 (2006).

77. Cheng, Y.-C. & Prusoff, W. H. Relationship between the inhibition constant (K1) and the concentration of inhibitor which causes 50 per cent inhibition (I50) of an enzymatic reaction. *Biochem Pharmacol* **22**, 3099–3108 (1973).

4.S1   Supplementary figures
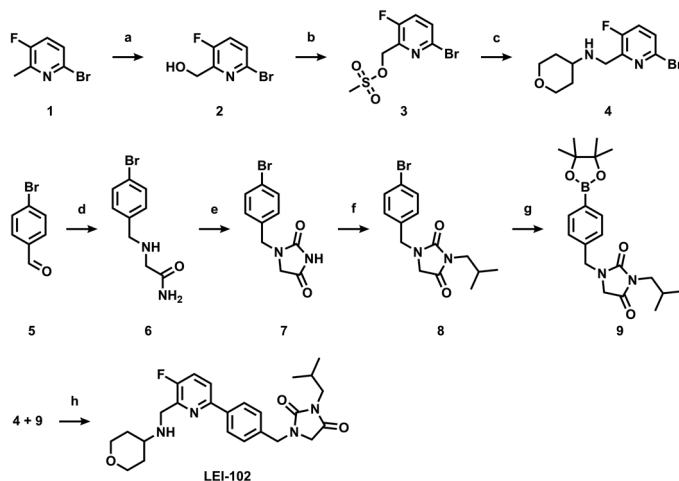
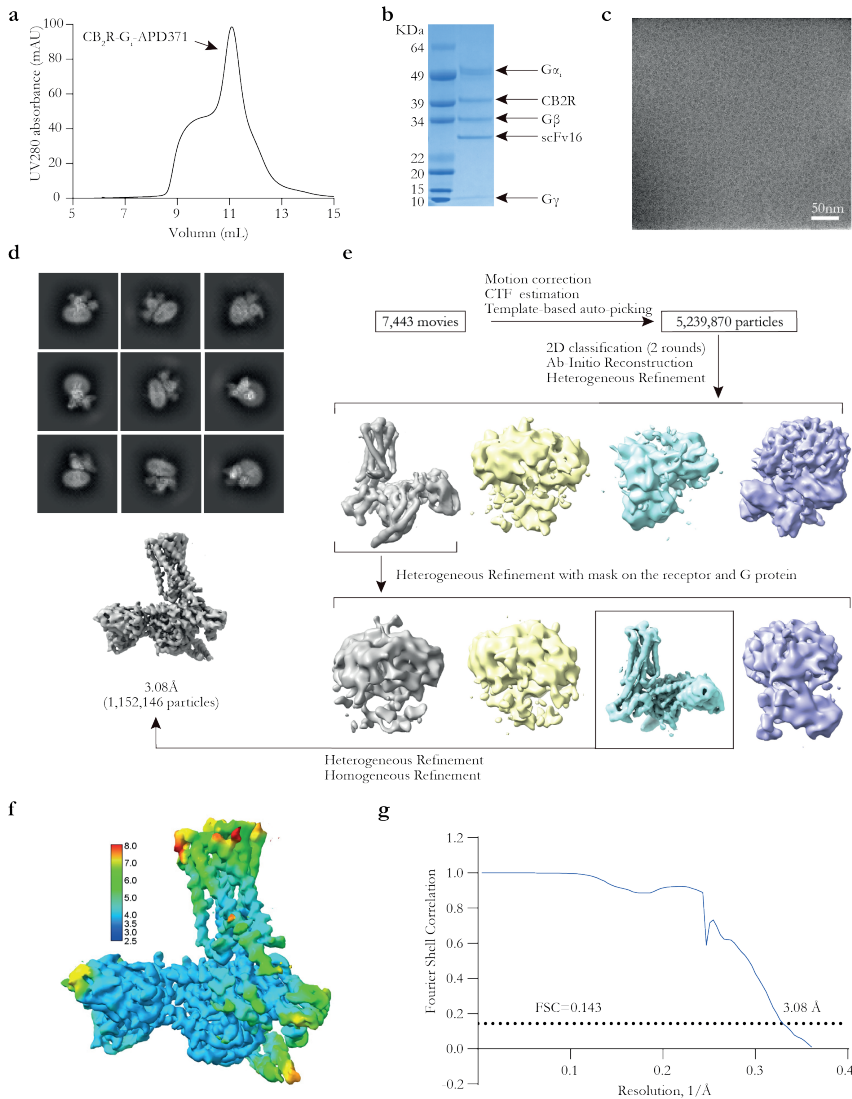**Figure 4.S1   Synthetic route of LEI-102.**

Reagents and conditions: a) step 1: m-CPBA (1.8 eq), 0 °C-rt, DCM, 4 days; step 2: TFAA (2.2 eq), 55 °C, 3 h; step 3: K_2CO_3 (2.4 eq), THF:MeOH (20:1), 17 h, 35% (three steps); b) Et_3N (2.3 eq), MsCl (1.7 eq), THF, 0 °C-rt, 1 h, 75%; c) K_2CO_3 (2.2 eq), tetrahydro-2H-pyran-4-amine (1.3 eq), ACN, 50 °C, 3 h, 67%; d) step 1: 2-aminoacetamide hydrochloride (1.0 eq), NaOH (1.1 eq), MeOH:H_2O (5:1), rt, 18 h; $NaBH_4$ (2.1 eq), 18 h, 91% (two steps); e) CDI (2.1 eq), DMAP (2.1 eq), ACN, 60 °C, 70 h, 37%; f) K_2CO_3 (3.0 eq), 1-bromo-2-methylpropane (2.0 eq), DMF, rt, 20 h, 88%; g) KOAc (4.4 eq), bis(pinacolato)diboron (1.5 eq), Pd(dppf)Cl2 (0.06 eq), DMF, 75 °C, 20 h; h) 4 (1.0 eq), 9 (1.5 eq), K_2CO_3 (6.0 eq), Pd(PPh_3)$_4$ (0.1 eq), toluene:EtOH (4:1), 75 °C, 18 h, 45% (two steps).

Chapter 4
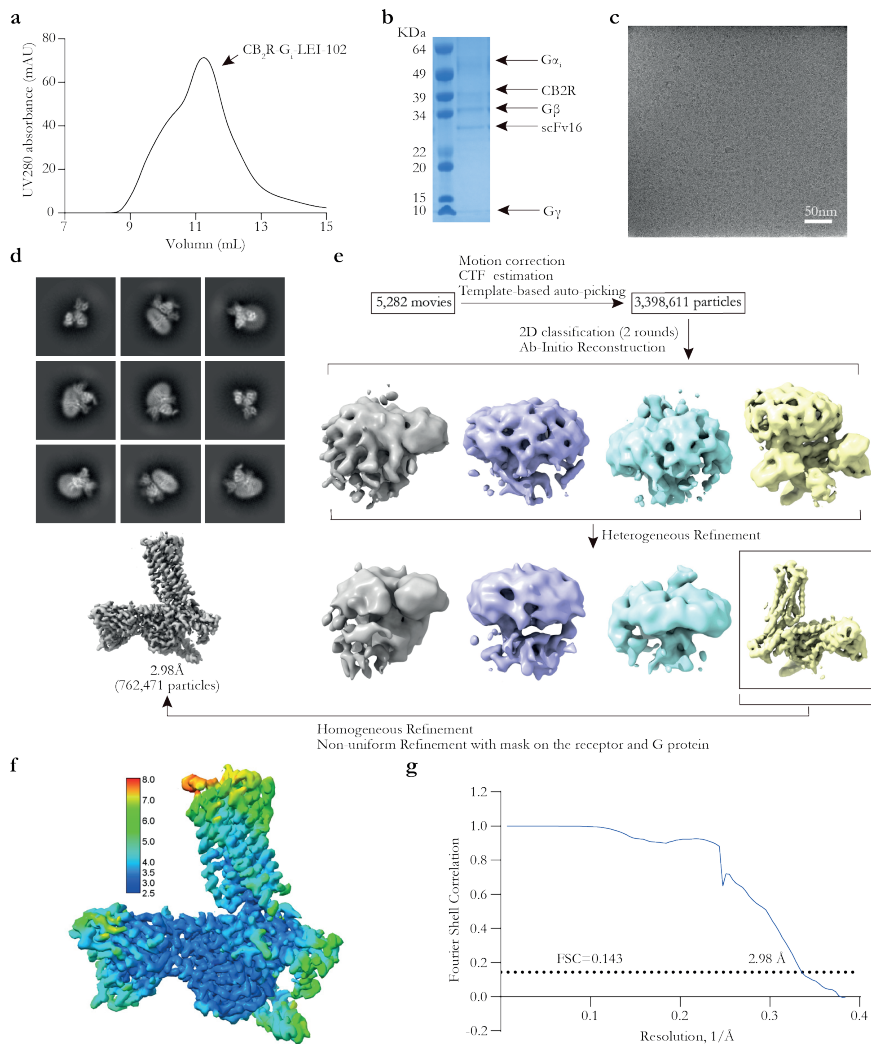
Figure 4.S2 **CB$_2$R-G$_i$-Scfv16-LEI-102 complex preparation and cryo-EM data processing.**
(a) Representative size-exclusion chromatography elution profile of CB$_2$R complex. Fractions corresponding to the main peak of monomers are indicated. (b) Coomassie blue staining of the CB$_2$R-G$_i$-scFv16 complex. (c) Representative cryo-EM micrograph of the CB$_2$R-G$_i$-scFv16 complex. Scale bar: 50 nm. (d) Representative 2D averages (box size: 256 Å) showing diverse secondary structure features. (e) Flow chart of cryo-EM single particle analysis of the CB$_2$R-G$_i$-scFv16 complex. (f) Local resolution map of the CB$_2$R-Gi-scFv16 complex. (g) Fourier shell correlation curves of the CB$_2$R-G$_i$-scFv16 complex.

Figure 4.S3 **CB$_2$R-G$_i$-Scfv16-APD371 complex preparation and cryo-EM data processing.**
(a) Representative size-exclusion chromatography elution profile of CB$_2$R complex. Fractions corresponding to the main peak of monomers are indicated. (b) Coomassie blue staining of the CB$_2$R-G$_i$-scFv16 complex. (c) Representative cryo-EM micrograph of the CB$_2$R-G$_i$-scFv16 complex. Scale bar: 50 nm. (d) Representative 2D averages (box size: 256 Å) showing diverse secondary structure features. (e) Flow chart of cryo-EM single particle analysis of the CB$_2$R-G$_i$-scFv16 complex. (f) Local resolution map of the CB$_2$R-Gi-scFv16 complex. (g) Fourier shell correlation curves of the CB$_2$R-G$_i$-scFv16 complex.
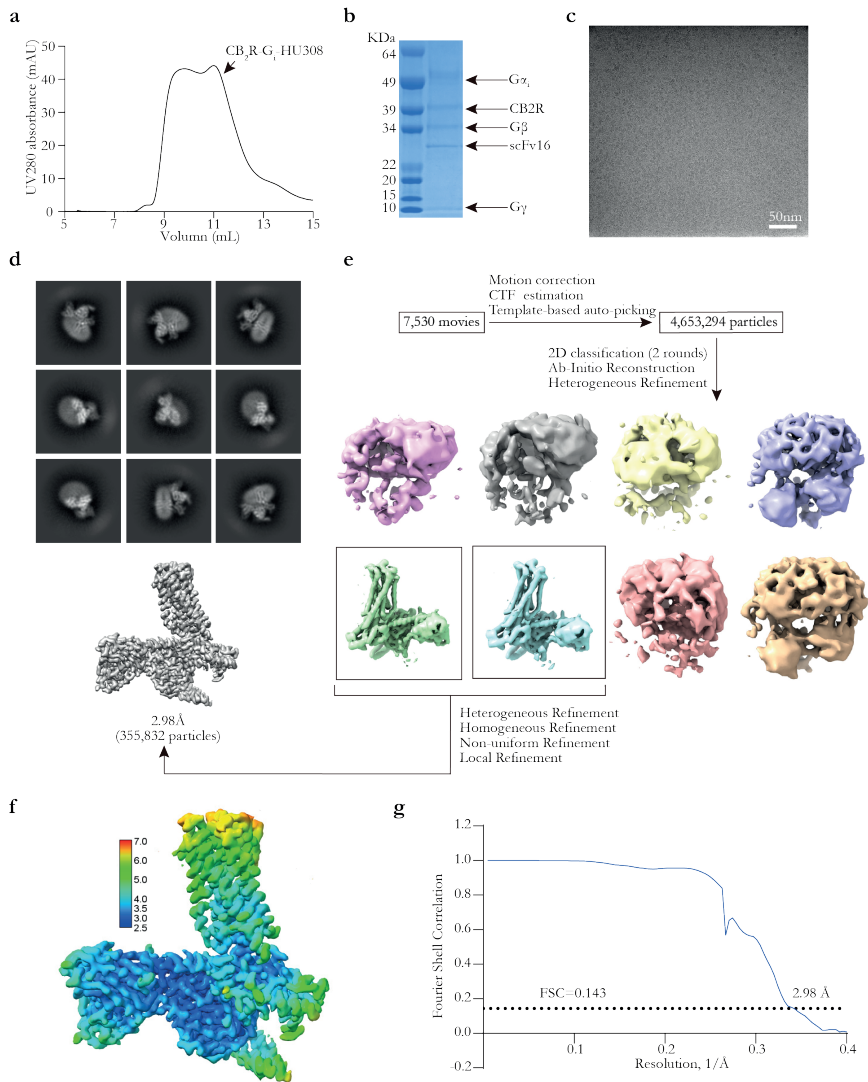
Figure 4.S4 **CB$_2$R-G$_i$-Scfv16-HU308 complex preparation and cryo-EM data processing.**
(a) Representative size-exclusion chromatography elution profile of CB$_2$R complex. Fractions corresponding to the main peak of monomers are indicated. (b) Coomassie blue staining of the CB$_2$R-G$_i$-scFv16 complex. (c) Representative cryo-EM micrograph of the CB$_2$R-G$_i$-scFv16 complex. Scale bar: 50 nm. (d) Representative 2D averages (box size: 256 Å) showing diverse secondary structure features. (e) Flow chart of cryo-EM single particle analysis of the CB$_2$R-G$_i$-scFv16 complex. (f) Local resolution map of the CB$_2$R-Gi-scFv16 complex. (g) Fourier shell correlation curves of the CB$_2$R-G$_i$-scFv16 complex.
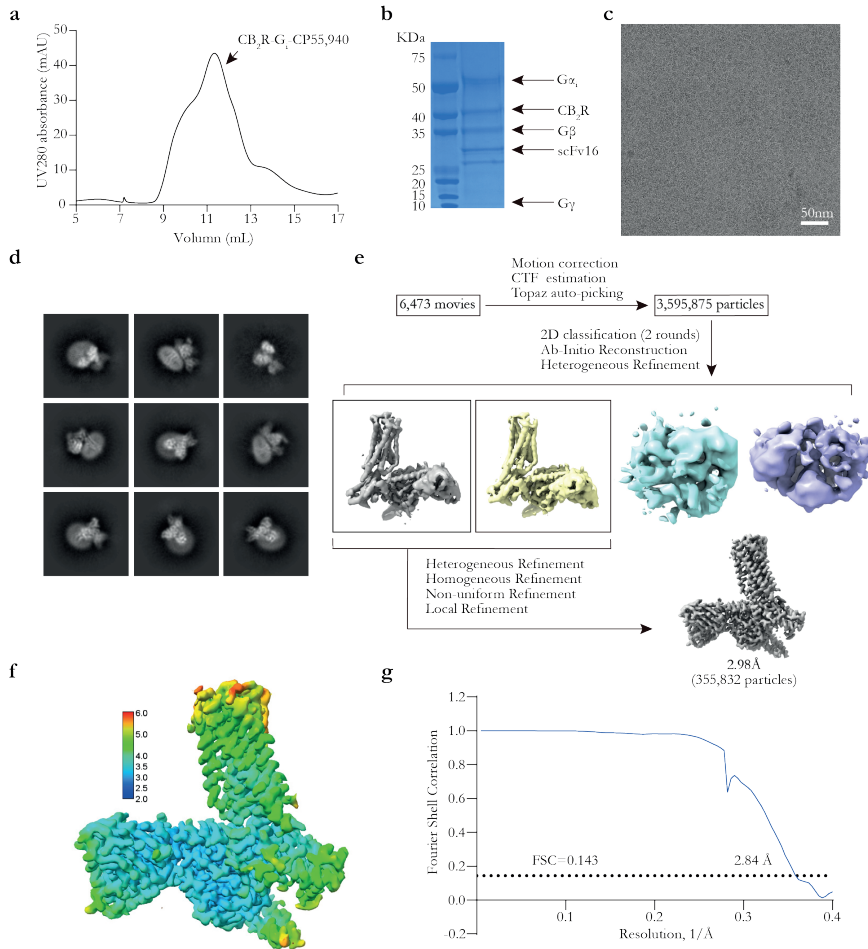
Figure 4.S5 **CB$_2$R-G$_i$-Scfv16-CP55,940 complex preparation and cryo-EM data processing.**
(a) Representative size-exclusion chromatography elution profile of CB$_2$R complex. Fractions corresponding to the main peak of monomers are indicated. (b) Coomassie blue staining of the CB$_2$R-G$_i$-scFv16 complex. (c) Representative cryo-EM micrograph of the CB$_2$R-G$_i$-scFv16 complex. Scale bar: 50 nm. (d) Representative 2D averages (box size: 256 Å) showing diverse secondary structure features. (e) Flow chart of cryo-EM single particle analysis of the CB$_2$R-G$_i$-scFv16 complex. (f) Local resolution map of the CB$_2$R-Gi-scFv16 complex. (g) Fourier shell correlation curves of the CB$_2$R-G$_i$-scFv16 complex.

a CB$_2$R-G$_i$-LEI-102 complex

TM1   TM2   TM3   TM4   TM5   TM6

TM7   ECL2   G$_i$H5   LEI-102

b CB$_2$R-G$_i$-APD371 complex

TM1   TM2   TM3   TM4   TM5   TM6

TM7   ECL2   G$_i$H5   APD371

c CB$_2$R-G$_i$-HU308 complex

TM1   TM2   TM3   TM4   TM5   TM6

TM7   ECL2   G$_i$H5   HU308

d CB$_2$R-G$_i$-CP55,940 complex

TM1   TM2   TM3   TM4   TM5   TM6

TM7   ECL2   G$_i$H5   CP55,940

Chapter 4

Figure 4.S6 **Representative cryo-EM density map of the CB$_2$R-G$_i$-scFv16 complex.**
(a-d) EM density map and models are shown for all transmembrane helices, ECL2, ligand and α5 helix of Gα$_i$ (G$_i$H5) in (a) LEI-102, (b) APD371, (c) HU308 and (d) CP55,940 bound CB$_2$R-G$_i$-scFv16 complex. Same color codes as in **Figure 4.2**.
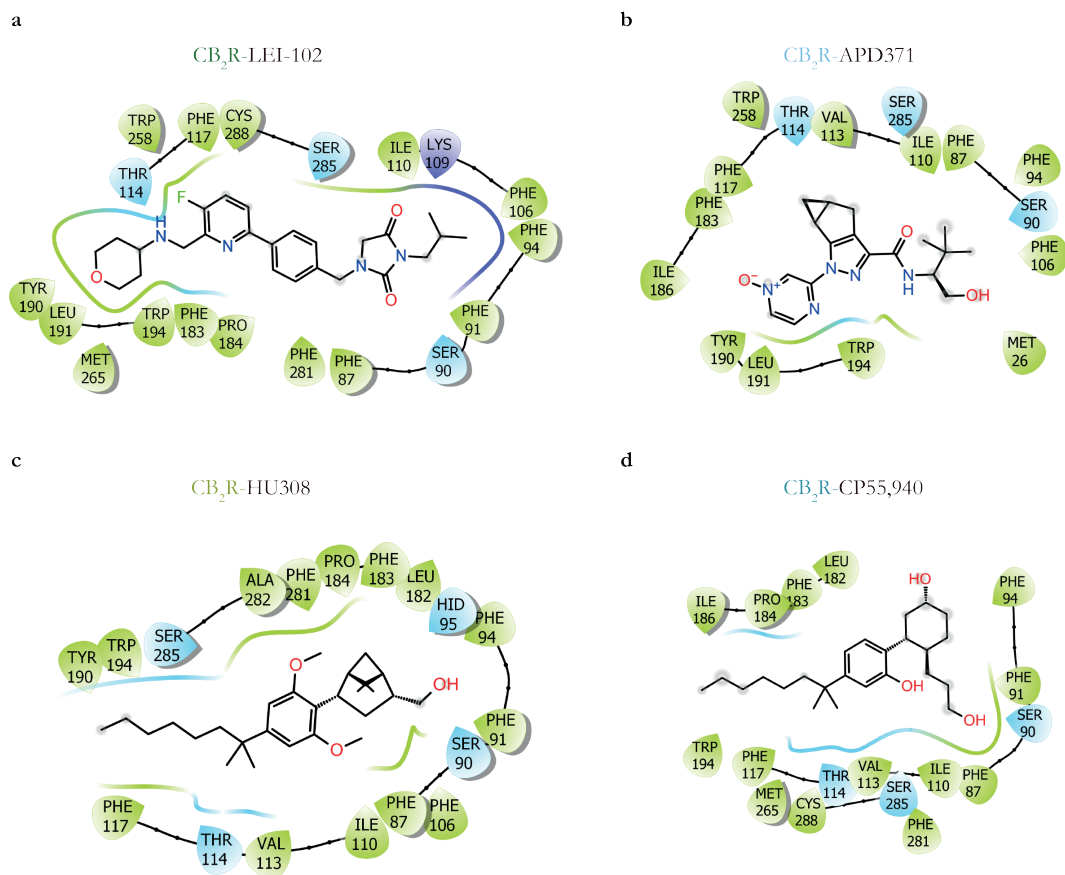
Figure 4.S7 **Schematic representation of interactions between CB$_2$R and agonists.**
(a-d) Schematic 2D representation of the binding pocket of agonist (a) LEI-102, (b) APD371, (c) HU308 and (d) CP55,940. Hydrophobic amino acids are colored in green, polar amino acids are colored in cyan, basic amino acids are colored in purple.
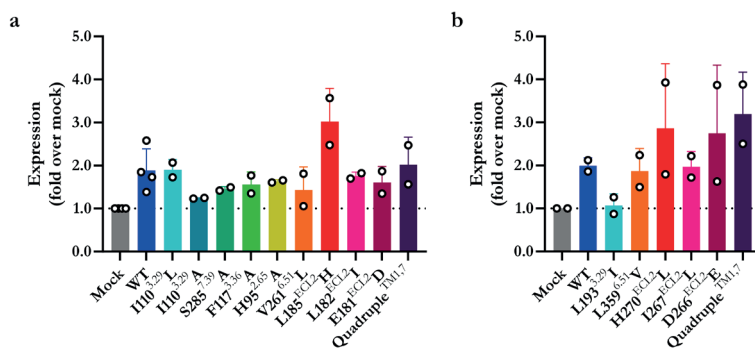
Figure 4.S8   **Cell surface receptor expression.**

Receptor expression as determined by ELISA for (a) CB_2R and (b) CB_1R WT and mutants. Data are expressed as mean ± SD of at least two experiments performed in quintuplicate.

4.S2   Supplementary tables

Table 4.S1   **Physico-chemical properties of the investigated ligands.**

Compound	cLogP	sLogP	TPSA (Å)	MW (g/mol)	Number Rotatable Bonds	Number HBD	Number HBA
Δ⁹-THC	7.24	5.74	29.5	314.5	4	1	2
2-AG	6.89	5.03	66.8	378.6	17	2	4
AEA	6.18	5.24	49.3	347.5	16	2	2
CP55,940	5.82	5.66	60.7	376.6	10	3	3
HU308	8.00	6.63	38.7	414.6	10	1	3
APD371	-0.35	0.70	107.0	357.4	4	2	6
LEI-102	2.07	3.58	74.8	454.5	8	1	5

All values were calculated using RDKit KNIME nodes version 4.5.0.v202207051536, apart from cLogP which was calculated using ChemDraw 19.0.

Chapter 4

Table 4.S2   Functional activity, affinity and kinetic parameters of synthetic agonists and endocannabinoids on hCB$_2$R.

Compound	pEC$_{50}$[a]	E$_{max}$ (%)[b]	pK$_i$ (K$_i$, nM)[c]	k$_{on}$ (M^{-1}s^{-1})[d]	ET (s)[e]	k$_{off}$ (s^{-1})[f]	RT (min)[g]	K$_D$ (nM)[h]
LEI-102	6.9 ± 0.2	76 ± 1	8.0 ± 0.1 (9.7)	(6.3 ± 1.1) × 10^4	16.0 ± 2.82	(1.0 ± 0.2) × 10^{-3}	16 ± 3.3	16.5
APD371	7.9 ± 0.1	134 ± 12	7.5 ± 0.1 (35.3)	(2.5 ± 0.4) × 10^4	40.1 ± 5.90	(3.7 ± 0.5) × 10^{-4}	45 ± 6.6	14.9
HU308	7.1 ± 0.2	91 ± 8	7.0 ± 0.1 (92.4)	(7.0 ± 2.3) × 10^3	143 ± 47.9	(2.3 ± 0.4) × 10^{-4}	71 ± 11	33.7
CP55,940	8.5 ± 0.3	98 ± 4	8.9 ± 0.1 (1.4)	(1.8 ± 0.4) × 10^6	0.57 ± 0.13	(5.2 ± 0.9) × 10^{-4}	32 ± 5.5	0.3
AEA	6.3 ± 0.2	60 ± 5	6.3 ± 0.1 (484.5)	(6.6 ± 0.5) × 10^3	152 ± 10.4	(2.4 ± 0.1) × 10^{-3}	6.8 ± 0.4	371.7
2-AG	5.9 ± 0.1	93 ± 22	7.0 ± 0.1 (97.3)	(5.3 ± 1.0) × 10^4	18.8 ± 3.61	(2.3 ± 0.3) × 10^{-3}	7.4 ± 1.0	42.7

[a, b] Potency (pEC$_{50}$) and efficacy (E$_{max}$) values were obtained from [^{35}S]GTPγS assays on HEK293T membranes transiently expressing CB$_2$R WT. The percentage maximum effect (E$_{max}$ in %) was calculated compared to CP55,940. [c, d, f] Binding affinities (pK$_i$), association (k$_{on}$) and dissociation (k$_{off}$) rate constants were determined in [^{3}H]RO6957022 binding assays on CHOK1_hCB$_2$bgal membranes at 10 °C. [e] Engagement time (ET) of the compound to the receptor at 1 µM agonist was determined by ET = 1/(k$_{on}$ · 1 × 10^{-6}) and is expressed in seconds (s), whereas k$_{on}$ is expressed in M^{-1}s^{-1}. [g] Residence time (RT) was determined by RT = 1/(60 · k$_{off}$) and is expressed in min, whereas k$_{off}$ is expressed in s^{-1}. [h] Kinetic K$_D$ values, defined by K$_D$ = k$_{off}$/k$_{on}$. Values represent the mean ± SEM of at least three independent experiments performed in duplicate .

Table 4.S3 **Characterization of cannabinoid CB$_1$ receptor mutations in [^{3}H]CP55,940 displacement assays.**

	Construct	pK$_D$ (K$_D$, nM)	LEI-102	APD371	HU308	CP55,940 pK$_i$[b]	AEA pK$_i$[b]	2-AG pK$_i$[b]
			Displacement (%)[a]					
BP	**WT**	8.3 ± 0.1 (5.24)	17 ± 7	-19 ± 17	6 ± 7	8.3 ± 0.1	6.3 ± 0.1	5.6 ± 0.2
	L193$^{3.29}$I	N.D.	N.D.	N.D.	N.D.	N.D.	N.D.	N.D.
	L359$^{6.51}$V	8.6 ± 0.2 (2.80)	25 ± 6	18 ± 9	41 ± 10	8.5 ± 0.1	6.3 ± 0.1	5.9 ± 0.1
Ligand entry	**H270^{ECL2}L**	8.4 ± 0.2 (3.70)	47 ± 5	8 ± 3	46 ± 3	8.4 ± 0.1	6.3 ± 0.0	5.5 ± 0.2
	I267^{ECL2}L	8.6 ± 0.1 (2.57)	25 ± 3	-24 ± 17	-7 ± 19	8.6 ± 0.1	6.4 ± 0.1	6.1 ± 0.2
	D266^{ECL2}E	8.7 ± 0.2 (1.91)	38 ± 10	12 ± 7	34 ± 5	8.7 ± 0.1	6.7 ± 0.1	5.9 ± 0.1
	Quadruple^{TM1,7}	8.1 ± 0.2 (8.36)	26 ± 10	0 ± 25	-13 ± 22	8.1 ± 0.2	6.4 ± 0.0	5.3 ± 0.0

Mutations are shown in the numbering of the cannabinoid CB$_1$ receptor (CB$_1$R) amino acid sequence, as well as the Ballesteros and Weinstein GPCR numbering system. [a,b] Percentage of [^{3}H]CP55,940 displacement by 10 μM compound or binding affinity (pK$_i$) were determined in [^{3}H]CP55,940 displacement assays on HEK293T membranes transiently expressing CB$_1$R constructs. All values are presented as the mean ± SEM of at least three independent experiments performed in duplicate. One-way Welch ANOVA with Dunnett's T3 posthoc test was used to analyze differences in pK$_D$ or pK$_i$ values compared to WT. N.D. is not determined. BP is binding pocket.

Table 4.S4   **Cryo-EM Data collection, model refinement, and validation statistics.**

	CB$_2$R-LEI-102-G$_i$	CB$_2$R-APD371-G$_i$	CB$_2$R-HU308-G$_i$	CB$_2$R-CP55,940-G$_i$
Data collection and processing				
Magnification	105,000	105,000	105,000	105,000
Voltage (kV)	300	300	300	300
Electron exposure (e–/Å^2)	60	60	60	60
Defocus range (µm)	-1.0~-2.0	-1.0~-2.0	-1.0~-2.0	-1.0~-2.0
Pixel size (Å)	0.52	0.52	0.52	0.52
Symmetry imposed	C1	C1	C1	C1
Images (no.)	5,282	7,443	7,530	6,473
Initial particle images (no.)	3,398,611	5,239,870	4,653,294	3,595,875
Final particle images (no.)	762,471	1,152,146	355,832	440,292
Map resolution (Å)	2.98	3.08	2.97	2.84
FSC threshold	0.143	0.143	0.143	0.143
Map resolution range (Å)	2.9~6.0	2.9~6.0	2.9~6.0	2.7~5.0
Refinement				
Initial model used (PDB code)	6KPF	6KPF	6KPF	6KPF
Map sharpening B factor (Å^2)	-104.2	-118.6	110.8	-100.9
Model composition				
Non-hydrogen atoms	8,812	8,801	8,817	8,888
Protein residues	1,137	1,137	1,137	1,139
Ligands	1	1	1	1
B factors (Å^2)				
Protein	68.00	61.04	68.91	68.22
Ligand	76.90	104.87	67.91	85.48
R.m.s. deviations				
Bond lengths (Å)	0.003	0.009	0006	0.010
Bond angles (°)	0.57	1.24	0.69	1.80
Validation				
MolProbity score	1.82	1.64	1.83	1.46
Clashscore	12.29	5.04	12.11	7.74
Poor rotamers (%)	0.00	0.32	0.00	0.00
Ramachandran plot				
Favored (%)	96.60	94.46	96.43	97.86
Allowed (%)	3.40	5.54	3.57	2.14
Disallowed (%)	0.00	0.00	0.00	0.00

Table 4.S5 Cell surface expression levels of cannabinoid receptor constructs in ELISA.

	CB$_2$R	Expression (fold over mock)	CB$_1$R	Expression (fold over mock)
	WT	1.9 ± 0.5	**WT**	2.0 ± 0.2
Binding pocket	**I110$^{3.29}$L**	1.9 ± 0.2	**L193$^{3.29}$I**	1.1 ± 0.3
	I110$^{3.29}$A	1.2 ± 0.0	**L193$^{3.29}$A**	N.D.
	S285$^{7.39}$A	1.5 ± 0.1	**S383$^{7.39}$A**	N.D.
	F117$^{3.36}$A	1.6 ± 0.3	**F200$^{3.36}$A**	N.D.
	H95$^{2.65}$A	1.6 ± 0.0	**H178$^{2.65}$A**	N.D.
	V261$^{6.51}$L	1.4 ± 0.5	**L359$^{6.51}$V**	1.9 ± 0.5
Ligand entry	**L185^{ECL2}H**	3.0 ± 0.8	**H270^{ECL2}L**	2.9 ± 1.5
	L182^{ECL2}I	1.8 ± 0.1	**I267^{ECL2}L**	2.0 ± 0.4
	E181^{ECL2}D	1.6 ± 0.4	**D266^{ECL2}E**	2.7 ± 1.6
	Quadruple^{TM1,7}	2.0 ± 0.6	**Quadruple^{TM1,7}**	3.2 ± 1.0

Mutations are shown in the numbering of the cannabinoid CB$_2$ (CB$_2$R) or CB$_1$ receptor (CB$_1$R) amino acid sequence as well as the Ballesteros and Weinstein GPCR numbering system. Data are presented as fold over mock (empty pcDNA3.1 vector) and are mean $\pm$ SD of at least two individual experiments performed in. N.D. is not determined.

Chapter 4

Table 4.S6 **Characterization of cannabinoid CB$_2$ receptor mutations in G protein activation assays.**

	Construct	Basal[a]	LEI-102			APD371		HU308	
			pEC$_{50}$[b]	E$_{max}$ (%)[c]		pEC$_{50}$	E$_{max}$ (%)	pEC$_{50}$	E$_{max}$ (%)
Binding pocket	**WT**	1.0 ± 0.0	6.9 ± 0.2	103 ± 3		7.9 ± 0.1	109 ± 3	7.1 ± 0.2	105 ± 3
	I110$^{3.29}$L	1.0 ± 0.0	7.8 ± 0.1**	91 ± 3		6.7 ± 0.3	101 ± 7	6.7 ± 0.4	122 ± 12
	I110$^{3.29}$A	1.0 ± 0.1	7.0 ± 0.6	36 ± 13		6.6 ± 0.6	28 ± 9**	6.4 ± 0.5	27 ± 10**
	S285$^{7.39}$A	0.9 ± 0.0	6.3 ± 0.3	45 ± 8*		6.5 ± 0.3	49 ± 6*	5.9 ±0.1***	65 ± 18
	F117$^{3.36}$A	0.8 ± 0.1	N.D.	11 ± 11		N.D.	2 ± 6**	N.D.	5 ± 11*
	H95$^{2.65}$A	0.9 ± 0.0	<5	64 ± 7		5.7 ± 0.2**	50±1****	6.6 ± 0.6	67 ± 16
	V261$^{6.51}$L	0.8 ± 0.0	6.4 ± 0.0	8 ± 4****		6.9 ± 0.2*	6 ± 2****	<5	26 ± 7**
Ligand entry	**L185^{ECL2}H**	1.2 ± 0.1	6.9 ± 0.1	217 ± 21		8.0 ± 0.1	183 ± 16	6.8 ± 0.2	146 ± 8
	L182^{ECL2}I	0.8 ± 0.0*	7.4 ± 0.8	11 ± 8*		6.6 ± 0.4	17 ± 4***	<5	10 ± 7**
	E181^{ECL2}D	0.9 ± 0.0	6.9 ± 0.6	28 ± 13		6.9 ± 0.6	39 ± 6**	7.0 ± 0.7	32 ± 3****
	Quadruple^{TM1,7}	0.9 ± 0.0	6.2 ± 0.2	27 ± 5**		8.4 ± 0.1	35 ± 7*	N.D.	1 ± 9*

← **Table 4.S6** *(continued)*

		CP55,940		AEA		2-AG	
	Construct	**pEC$_{50}$**	**E$_{max}$ (%)**	**pEC$_{50}$**	**E$_{max}$ (%)**	**pEC$_{50}$**	**E$_{max}$ (%)**
Binding pocket	**WT**	8.5 ± 0.3	99 ± 3	6.3 ± 0.2	106 ± 7	5.9 ± 0.1	85 ± 2
	I110$^{3.29}$L	9.4 ± 0.2	96 ± 3	N.D.	N.D.	N.D.	N.D.
	I110$^{3.29}$A	8.7 ± 0.4	30 ± 2****	N.D.	N.D.	N.D.	N.D.
	S285$^{7.39}$A	6.7 ± 0.1**	25 ± 5**	N.D.	N.D.	N.D.	N.D.
	F117$^{3.36}$A	N.D.	-1 ± 14	N.D.	N.D.	N.D.	N.D.
	H95$^{2.65}$A	6.9 ± 0.2**	68 ± 11	N.D.	N.D.	N.D.	N.D.
	V261$^{6.51}$L	<5	12 ± 7**	N.D.	N.D.	N.D.	N.D.
Ligand entry	**L185^{ECL2}H**	8.9 ± 0.4	142 ± 16	6.6 ± 0.0	210 ± 61	5.9 ± 0.2	171 ± 16
	L182^{ECL2}I	8.8 ± 0.8	19 ± 2****	<5	5 ± 17*	<5	15 ± 9*
	E181^{ECL2}D	7.9 ± 0.5	19 ± 10	<5	14 ± 5**	<5	22 ± 15
	Quadruple^{TM1,7}	8.1 ± 0.2	18 ± 14	<5	24 ± 7**	<5	6 ± 4***

Mutations are shown in the numbering of the cannabinoid CB$_2$ receptor (CB$_2$R) amino acid sequence as well as the Ballesteros and Weinstein GPCR numbering system. [a,b,c] Basal activity, potency (pEC$_{50}$) and efficacy (E$_{max}$) values were obtained from [^{35}S]GTPγS assays on HEK293T membranes transiently expressing CB$_2$R constructs. The percentage maximum effect at 10 μM (E$_{max}$ in %) and the fold basal activity values were calculated compared to WT. pEC$_{50}$ <5 was reported when the curve fit was not finished. Binding pocket mutations were not assessed for endocannabinoids. Values are presented as the mean ± SEM of at least three independent experiments performed in duplicate. One-way Welch ANOVA with Dunnett's T3 posthoc test or Welch's t-test was used to analyze differences in pEC$_{50}$ and E$_{max}$ values compared to WT (*$p < 0.05$, ** $p < 0.01$, *** $p < 0.001$, **** $p < 0.00001$). N.D. is not determined.

Chapter 4

Table 4.S7   Characterization of cannabinoid CB$_2$ receptor mutations in [^{3}H]CP55,940 displacement assays.

	Construct	pK$_D$ (K$_D$, nM)^a	LEI-102 pK$_i$^{b}	APD371 pK$_i$^{b}	HU308 pK$_i$^{b}	CP55,940 pK$_i$^{b}	AEA pK$_i$^{b}	2-AG pK$_i$^{b}
BP	**WT**	9.1 ± 0.0 (0.77)	7.5 ± 0.1	8.0 ± 0.0	7.8 ± 0.2	9.2 ± 0.2	6.2 ± 0.1	5.8 ± 0.1
	I110$^{3.29}$L	9.2 ± 0.2 (0.66)	7.9 ± 0.0	7.1 ± 0.0***	7.3 ± 0.1	9.1 ± 0.1	6.1 ± 0.1	5.8 ± 0.1
Ligand entry	**L185^{ECL2}H**	9.2 ± 0.1 (0.60)	7.3 ± 0.1	7.7 ± 0.1	7.2 ± 0.0	9.4 ± 0.1	6.3 ± 0.1	6.4 ± 0.2
	Quadruple^{TM1,7}	9.0 ± 0.1 (1.08)	6.8 ± 0.2	6.7 ± 0.3	7.1 ± 0.4	9.2 ± 0.1	5.6 ± 0.3	<5

Mutations are shown in the numbering of the cannabinoid CB$_2$ receptor (CB$_2$R) amino acid sequence as well as the Ballesteros and Weinstein GPCR numbering system. ^{a,b} Binding affinities (pK$_D$, pK$_i$) were determined in [^{3}H]CP55,940 displacement assays on HEK293T membranes transiently expressing CB$_2$R constructs. pK$_i$ <5 was reported when the curve fit was not finished. All values are presented as the mean ± SEM of at least three independent experiments performed in duplicate. One-way Welch ANOVA with Dunnett's T3 posthoc test was used to analyze differences in pK$_i$ values compared to WT (*p < 0.05, ** p < 0.01, *** p < 0.001). Mutations I110$^{3.29}$L, S285$^{7.39}$A, F117$^{3.36}$A, H95$^{2.65}$A, V261$^{6.51}$L, L185^{ECL2}I and E181^{ECL2}D could not be assessed due to lack of specific binding window. BP is binding pocket.

Table 4.S8   Characterization of cannabinoid CB$_1$ receptor mutations in G protein activation assays.

	Construct	Basal^a	LEI-102	APD371	HU308	CP55,940	AEA	2-AG
BP	**WT**	1.0 ± 0.0	1.0 ± 0.1	1.0 ± 0.0	0.8 ± 0.0	1.2 ± 0.1	1.2 ± 0.1	1.3 ± 0.1
	L193$^{3.29}$I	N.D.	N.D.	N.D.	N.D.	N.D.	N.D.	N.D.
	L359$^{6.51}$V	0.7 ± 0.0*	1.1 ± 0.1	1.1 ± 0.1	0.9 ± 0.1	1.4 ± 0.2	1.4 ± 0.2	1.4 ± 0.2
Ligand entry	**H270^{ECL2}L**	0.7 ± 0.0**	1.2 ± 0.0	1.1 ± 0.0	1.2 ± 0.1*	1.6 ± 0.1	1.4 ± 0.1	1.5 ± 0.1
	I267^{ECL2}L	1.1 ± 0.0	1.0 ± 0.0	0.9 ± 0.0	0.8 ± 0.0	1.0 ± 0.0	1.0 ± 0.1	1.1 ± 0.0
	D266^{ECL2}E	0.7 ± 0.0**	1.1 ± 0.1	0.9 ± 0.1	0.8 ± 0.1	1.4 ± 0.1	1.3 ± 0.1	1.5 ± 0.2
	Quadruple^{TM1,7}	0.6 ± 0.1**	1.2 ± 0.1	1.1 ± 0.0	0.9 ± 0.0	1.8 ± 0.1*	1.6 ± 0.1	1.8 ± 0.1*

Mutations are shown in the numbering of the cannabinoid CB$_1$ receptor (CB$_1$R) amino acid sequence as well as the Ballesteros and Weinstein GPCR numbering system. ^{a} Basal activity is expressed as fold over WT. Agonist-mediated activation values were obtained from [^{35}S]GTPγS assays on HEK293T membranes transiently expressing CB$_1$R constructs using 10 μM agonist, and are expressed as fold over its basal. Values are presented as the mean ± SEM of three independent experiments performed in duplicate (*n* indicates the number of biological replicates). One-way Welch ANOVA with Dunnett's T3 posthoc test was used to analyze differences in activation values compared to WT (*p < 0.05, ** p < 0.01, *** p < 0.001, **** p < 0.00001). Exact p values are given between square brackets. N.D. is not determined. BP is binding pocket.